

Turn-key super-resolution mapping of cell receptor force orientation and magnitude using a commercial structured illumination microscope

Aaron Blanchard

Emory University

J. Dale Combs

Emory University

Joshua Brockman

Emory University

Anna Kellner

Emory University

Roxanne Glazier

Emory University

Hanquan Su

Emory University

Rachel Bender

Emory University

Alisina Bazrafshan

Emory University

Wenchun Chen

Emory University

M Quach

Emory University

Renhao Li

Emory University <https://orcid.org/0000-0002-5806-5080>

Alexa Mattheyses

University of Alabama at Birmingham <https://orcid.org/0000-0002-5119-7750>

Khalid Salaita (✉ k.salaita@emory.edu)

Emory University <https://orcid.org/0000-0003-4138-3477>

Article

Keywords: Nanoscale Biophysics, Biosensors, Polarization microscopy, Integrins, Super-resolution Microscopy

Posted Date: October 7th, 2020

DOI: <https://doi.org/10.21203/rs.3.rs-83810/v1>

License:  This work is licensed under a Creative Commons Attribution 4.0 International License.

[Read Full License](#)

Version of Record: A version of this preprint was published at Nature Communications on August 3rd, 2021. See the published version at <https://doi.org/10.1038/s41467-021-24602-x>.

Turn-key super-resolution mapping of cell receptor force orientation and magnitude using a commercial structured illumination microscope

Aaron Blanchard¹, Dale J. Combs², Joshua M. Brockman¹, Anna V. Kellner¹, Roxanne Glazier¹, Hanquan Su², Rachel L. Bender², Alisina Bazrafshan², Wenchun Chen^{3,4}, M. Edward Quach^{3,4}, Renhao Li^{3,4}, Alexa L. Mattheyses⁵, & Khalid Salaita^{1,2,}*

¹Wallace H. Coulter Department of Biomedical Engineering, Georgia Institute of Technology and Emory University, Atlanta, Georgia 30322, USA

²Department of Chemistry, Emory University, 1515 Dickey Drive, Atlanta, Georgia 30322, USA

³Aflac Cancer and Blood Disorders Center, Children's Healthcare of Atlanta,

⁴Department of Pediatrics, Emory University School of Medicine

⁵Department of Cell, Developmental, and Integrative Biology, University of Alabama at Birmingham, Birmingham, Alabama, 35294, USA

*Address correspondence to: k.salaita@emory.edu

Abstract

Many cellular processes, including cell division, development, and cell migration require spatially and temporally coordinated forces transduced by cell surface receptors. Nucleic acid-based molecular tension probes allow one to quantify and visualize the piconewton (pN) forces applied by these receptors. Building on this technology, we recently imaged DNA tension probes using fluorescence polarization imaging to map the magnitude and 3D orientation of receptor forces with diffraction limited resolution (~250 nm). Further improvements in spatial resolution are desirable as many force-sensing receptors are organized at the nano-scale in supramolecular complexes such as focal adhesions. Here, we show that structured illumination microscopy (SIM), a super-resolution technique, can be used to perform super-resolution molecular force microscopy (MFM). Using SIM-MFM, we generate the highest resolution maps of both the magnitude and orientation of the pN traction forces applied by cells. We apply SIM-MFM to map platelet and fibroblast integrins forces, as well as T cell receptor forces. The method reveals that platelets dynamically re-arrange the orientation of their integrin forces during activation. Monte Carlo simulations validated the results and provided analysis of the sources of noise. Importantly, we envision

that SIM-MFM will be broadly adopted by the cell biology and mechanobiology communities because it can be implemented on any standard SIM microscope without hardware modifications.

Introduction

Cellular forces are generated by the cytoskeleton and then transmitted through membrane receptors to other cells and the extracellular matrix. These pN forces are critical for maintaining a wide variety of essential processes in mammalian cells, including development, migration, immune recognition, and coagulation¹⁻⁷. Over nearly a decade, our group has developed an array of molecular tension fluorescence microscopy (MTFM) probes for quantifying and visualizing the pN-scale molecular forces transmitted by cell surface receptors^{4,8-18}. These probes consist of an extensible “molecular spring” flanked by a fluorophore-quencher pair and are generally conjugated to a substrate such as a glass coverslip^{8,10,11,16,19,20} or lipid membrane^{21,22}. The MTFM probes present peptide or protein ligands that are recognized by cell receptors (e.g. integrins). When the cellular receptor applies sufficient force, the MTFM probes will unfold and extend, resulting in dequenching of the fluorophore and a marked increase in fluorescence, a signal that can be imaged in space and time using conventional fluorescence microscopy (**Fig. 1a**).

Compared to traction force microscopy (TFM), the gold standard technique for measuring cellular tractions, MTFM offers a significant improvement in spatial resolution ($\sim 0.25 \mu\text{m}$ versus $\sim \mu\text{m}$) and three orders-of-magnitude improvement in force magnitude resolution (pN versus nN)⁸. Hence, MTFM is attracting the interest of the cell biology community²³⁻²⁵. Nonetheless, an important distinction between MTFM and TFM is that the former is used to report on force magnitude, without reporting on force orientation. This is indeed a limitation, as recent work has increasingly shown that force orientation, not only force magnitude, is transduced into biochemical signals. For example, the T-cell receptor (TCR), integrins, and vinculin have been shown to be orientation-dependent mechanosensors^{3,4,26}. In addition to orientation, recent super-resolution work has shown the importance of nanoscale organization of force-bearing structures^{18,27}. Many physiologically-important force-bearing structures – such as focal adhesions⁸, lamellipodial protrusions⁴, T-cell receptor clusters¹⁷, and podosomes^{22,28} – are hundreds or tens of

nanometers (nm) in their smallest dimension and also generate highly oriented forces. Thus, tools for super-resolution MTFM that also report on force orientation are highly desirable.

We recently took advantage of fluorescence polarization imaging to report on the force orientation of molecular probes¹⁶. This approach, dubbed molecular force microscopy (MFM), is enabled by the combination of DNA mechanotechnology²⁹-based tension probes – which include DNA hairpins as their “molecular springs” – with excitation-resolved fluorescence polarization microscopy³⁰⁻⁴⁰. DNA hairpins are well-suited for molecular force measurement because they offer a nearly-“digital” force response; a DNA hairpin can exist in one of two states – folded or unfolded – and the fraction of time spent in the folded state decreases from ~95% to ~5% over a narrow force range of 2-3 piconewtons (pN) centered around the probe’s $F_{1/2}$ (defined as the force where the probe spends equal time in each state). $F_{1/2}$ can be tuned from ~2 pN to ~19 pN by adjusting the length and GC content of the hairpin⁴¹. Due to highly efficient quenching, the fluorescence intensity of the opened state is ~20-100x brighter than that of the closed state⁸.

The fluorophore most commonly used in DNA hairpin probes, cyanine 3b (Cy3b), has two properties that make MFM possible: First, Cy3b, like most fluorophores, has a transition dipole moment that can be approximated as a 3-dimensional (3D) vector, $\boldsymbol{\mu}$ (**Fig. 1b**)^{16,42}. (The transition dipole moments for excitation and emission are highly similar for Cy3b, and can thus be approximated as a single vector¹⁶). The intensity (I) of a fluorophore excited by plane-polarized excitation light (which has a fixed polarization vector denoted by \boldsymbol{E}) can be described by the relationship:

$$I \propto \langle \cos^2(\psi) \rangle \quad (1)$$

where ψ is the angle between $\boldsymbol{\mu}$ and \boldsymbol{E} and $\langle \rangle$ denote ensemble averaging across the probability distribution of orientations that $\boldsymbol{\mu}$ and \boldsymbol{E} adopt over time. When \boldsymbol{E} is rotated (e.g. by placing a rotatable half wave plate in the path of the excitation beam) and multiple images of a sample are taken with different fixed \boldsymbol{E} orientations, the set of I values recorded for each pixel can be used to calculate the average fluorophore orientation in the physical region corresponding to that pixel.

Second, when Cy3b is covalently coupled to the terminus of a DNA duplex, it inherently stacks perpendicular to the duplex's long-axis⁴³. This property, and the nature of our tension probe design, cause Cy3b to align itself such that μ is perpendicular to the long axis of the opened probe (**Fig. 1b**). Because probe orientation is controlled by receptor-ligand force orientation, μ is therefore perpendicular to the force vector F . We assume that the probe can freely rotate around its long axis thanks to the incorporation of flexible linkers flanking the probe. Accordingly, μ can take an ensemble “disk” of orientations perpendicular to F (**Fig. 1b**). In this scenario, fluorescence intensity can be described by the equation:

$$I = A \sin^2(\alpha - \phi) + c \quad (4)$$

where ϕ and α are the in-plane angles of the F and E , respectively (**Fig. 1b**) and A and c are the sinusoid's amplitude and offset and depend on factors such as the tilt angle of the force, θ (**Fig. 1b**), and the surface density of opened tension probes. Note that α is the independent, user-controlled variable while ϕ , c , and A are the parameters being measured. We previously derived¹⁶ an equation to roughly calculate θ :

$$\theta = \cos^{-1} \left(\sqrt{\frac{\frac{c}{A+c} - b}{1-b}} \right) \quad (5).$$

where b – which we previously estimated to be 0.069 – is used to account for the estimate that the fluorophore spends ~10% of its time unstacked from the duplex terminus (during which time the fluorophore is randomly oriented)⁴³.

In our initial implementation of MFM¹⁶, we utilized a rotating half wave plate to vary α continuously and recorded a series of 73 images over the course of ~3.2 seconds. We then used least-squares residuals fitting to fit the intensity values for each pixel to equation (4). Because eqn. (4) has three unknown fit parameters (ϕ , θ , and A), three unique α values (e.g. $\alpha = 0^\circ$, 60° , and 120°) would technically be sufficient to obtain a unique best-fit curve analytically (**Fig. 1c**).

As stated above, enhancing the spatial resolution of MFM is desirable due to the nanoscale size of many mechanically active structures of interest. While we recently developed a method for localization of integrin forces with a spatial resolution of ~ 20 nm, this method does not capture force orientation information¹⁸. An additional limitation of MFM is the requirement for a microscope setup where α can be modulated freely. However, this is not a standard feature in the vast majority of commercially-available fluorescence microscopes. As a result, MFM is technologically inaccessible to a large proportion of the cell biology community.

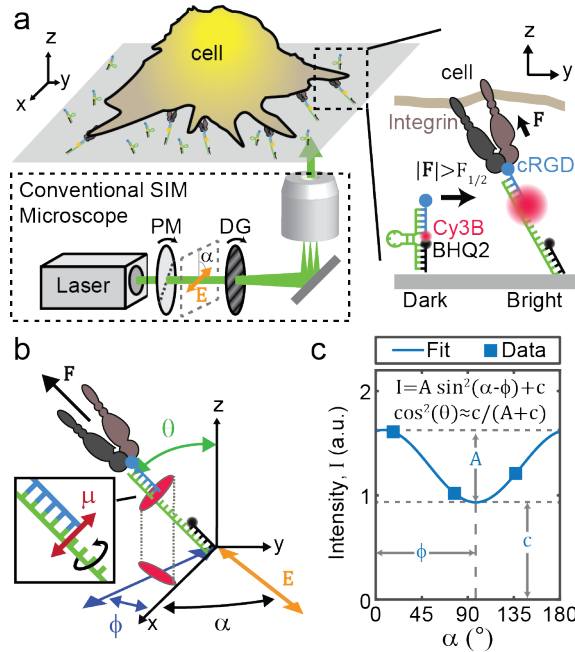


Figure 1: SIM-MFM concept **a)** Diagram showing microscope setup and DNA hairpin-based tension probe function. We show the basic components of a SIM microscope excitation line: a linearly-polarized laser passes through a polarization modulator (PM) and diffraction grating (DG). These two components rotate together such that α (the angle of the laser beam's electric field vector, E) is the same as the orientation of the striping pattern created by the DG. Inset shows a DNA hairpin-based tension probe (blue, green, and black DNA strands) transitioning from a closed state to an opened state upon application of tension (F) with a magnitude exceeding the probe's $F_{1/2}$ value. Cell receptor (brown and gray) is an integrin and the ligand (blue circle) is cRGD. **b)** Illustration of F (black arrow) and E (orange dipole) angles used in this work. Inset shows Cy3b transition dipole moment (μ) perpendicular to the long axis of the tension probe. **c)** Representative data and curve fit from a pixel indicated in Fig. 2c (green arrow). A , c , and ϕ are illustrated and the equations used to obtain curve fit from data are shown.

Recently, Zhanghao *et. al* reported a technique called polarized structured illumination microscopy (pSIM), which can be used to map fluorophore orientation with high spatial resolution (~ 100 nm) and fast temporal resolution (< 1 second)⁴⁴. Inspired by this recent development, here we report the successful adaptation of pSIM to MFM¹⁶ to generate ~ 100 nm resolution maps of the pN magnitudes and orientations of forces generated by living cells. We call this technique SIM-MFM. The significance of this advance is that we simultaneously address the spatial resolution and the accessibility of MFM using a commercially available microscope. SIM is an increasingly-utilized super-resolution fluorescence imaging modality that achieves ~ 100 nm spatial resolution by exciting fluorescent samples with a structured pattern of excitation light. Many research institutions maintain SIM microscopes within core facilities or within a small number of research labs. Importantly, SIM-MFM can be implemented in a turn-key fashion without any hardware or software modifications to the imaging system.

Results

Proof-of-concept demonstration of SIM-enabled MFM.

The SIM technique fundamentally depends on polarization modulation, which conveniently coincides with the optical requirements for performing MFM (**Fig. 1a**). Specifically, SIM⁴⁵⁻⁴⁸ works by using a diffraction grating to create an excitation beam illumination pattern that varies sinusoidally in one dimension. The sinusoidal interference pattern is then shifted back and forth, generally for a total of three or five images with different phase shifts. The orientation of the illumination pattern is then rotated and this process is repeated at two or more distinct illumination pattern angles, resulting in a minimum of nine images (if three phase shifts per stripe orientation are used) or fifteen images (if five phase shifts per stripe orientation are used). These images are then processed using a reconstruction algorithm to produce a single image with an improvement in spatial resolution when compared to widefield epifluorescence. Importantly, the sinusoidal diffraction pattern can only form properly when excitation light is linearly polarized with \mathbf{E} parallel to the striping orientation. Therefore, when the striping orientation is modulated, so is α (**Fig. 1a**). Accordingly, polarization modulation is a fundamental and enabling characteristic of SIM.

To test whether SIM could be used to implement MFM, we first verified the inherent polarization modulation of our SIM microscope by imaging a standard control: microspheres coated with tetramethylindocarbocyanine (DiI)-doped supported lipid bilayers. DiI is a cyanine dye (similar to Cy3b) linked to two lipid tails that spontaneously insert into supported lipid bilayers such that μ should be tangential to the microsphere surface. As expected, we observed a sinusoidal variation in I around the perimeter of the microsphere, with maximal intensity corresponding to the spot where μ was aligned with the striping pattern (**Fig S1**). As α varied during each SIM acquisition, the sinusoid shifted by a commensurate amount, thus confirming that the polarization modulates with the direction of the stripe pattern for our commercial SIM microscope at an interval of $\sim 60^\circ$. Each full set of images was collected in ~ 1 sec – notably more rapid than the previous implementation of MFM¹⁶ which required ~ 3.6 sec per acquisition.

We next tested whether SIM could be used to implement MFM. To do this, we prepared a typical DNA hairpin-based MTFM experiment by conjugating DNA tension probes ($F_{1/2} = 4.7$ pN) presenting cyclic arginine-glycine-aspartic acid-*D*-phenylalanine-lysine (cRGDfK, a peptide that binds $\alpha_v\beta_3$ and $\alpha_5\beta_1$ integrin receptors with high affinity⁴⁹) to a glass coverslip through biotin-streptavidin binding. Previous surface density calibration of surfaces prepared in this manner¹⁶ revealed a density of ~ 700 tension probes per μm^2 . We next deposited quiescent human platelets on these surfaces. We used platelets as a model because they are small and highly mechanically active, and because integrin mechanics are important in platelet physiology⁵⁰. Indeed, resolving the spatial distribution of mechanical platelet traction forces is very challenging for state-of-the-art traction force microscopy due to their small size ($\sim 2\text{-}5$ μm spread diameter)^{4,16,51-53}.

Within $\sim 10\text{-}20$ minutes of seeding, platelets engaged and spread on the surface. Binding of platelet integrins to cRGDfK ligands promoted outside-in integrin activation and initiated platelet signaling,

spreading, and cytoskeletal remodeling – ultimately leading to transmission of forces through the integrin-ligand bond and opening of the tension probe⁴. We then collected SIM images of well-spread platelets within ~45 minutes. Typically, platelets spread out over an area ~2 – 5 μm in width and their MTFM maps generally exhibited two distinct features: an outer ring of tension, which coincides with actin polymerization at the lamellipodial edge of the cell, and a large inner region with lobes of tension, which arises from actomyosin activity in the body of the platelet. The tension patterns observed here were consistent with those observed in our prior work^{4,16,18} validating the rigor and reproducibility of the probe and the biological model (**Fig. 2, S2-3**).

We next tested to see whether the polarization modulation of the SIM microscope could be used to measure force orientation. For our initial assessment, we used the built-in “3D-SIM” function of our Nikon Eclipse Ti-based commercial SIM microscope to acquire three sets of five images (**Fig. 2a** – five phase shifts at each of three striping orientations). We then simply took the average of the images acquired at each striping orientation (this is mathematically valid due to the specific phase shifts used in SIM), resulting in three images each corresponding to a unique α value such that each pixel has three intensity values associated with it (**Fig. 1c**). We then loaded the image into fairSIM⁵⁴ (an open-source ImageJ plugin that enables facile analysis of SIM data), which revealed striping orientations (and therefore α values) of 77° , 137° , and 17° . Accordingly, for a given pixel we designate the three respective intensity averages as I_{17° , I_{77° , and I_{137° . Rather than applying least squares residuals fitting to the I vs. α curve as performed previously¹⁶, we derived analytical equations (**Supplemental Note 1**) to rapidly obtain a unique fit to equation 4 for each pixel:

$$\phi = \frac{1}{2} \tan^{-1} \left(\frac{I_{avg} - I_{137^\circ} - (I_{avg} - I_{77^\circ}) \cos(120^\circ)}{(I_{avg} - I_{137^\circ}) \sin(120^\circ)} \right) + 77^\circ \quad (6a).$$

$$A = \frac{2(I_{avg} - I_{137^\circ})}{\cos(2(77^\circ - \phi))} \quad (6b).$$

$$c = I_{77^\circ} - A \sin^2(77^\circ - \phi) \quad (6c).$$

$$\theta = \cos^{-1} \left(\sqrt{\frac{\frac{I_{max}}{c} - 0.069}{1 - 0.069}} \right) \quad (6d),$$

Where I_{max} is the maximum intensity of the fit sinusoid:

$$I_{max} = A + c \quad (7)$$

which is a better metric for brightness than I_{avg} because I_{max} is (very nearly) proportional to the number of opened probes regardless of force orientation. We then applied these calculations to the entire image set. Our initial results reproduced the force patterns that are expected for platelets, demonstrating that SIM-MFM is viable (**Figure 2b-e**).

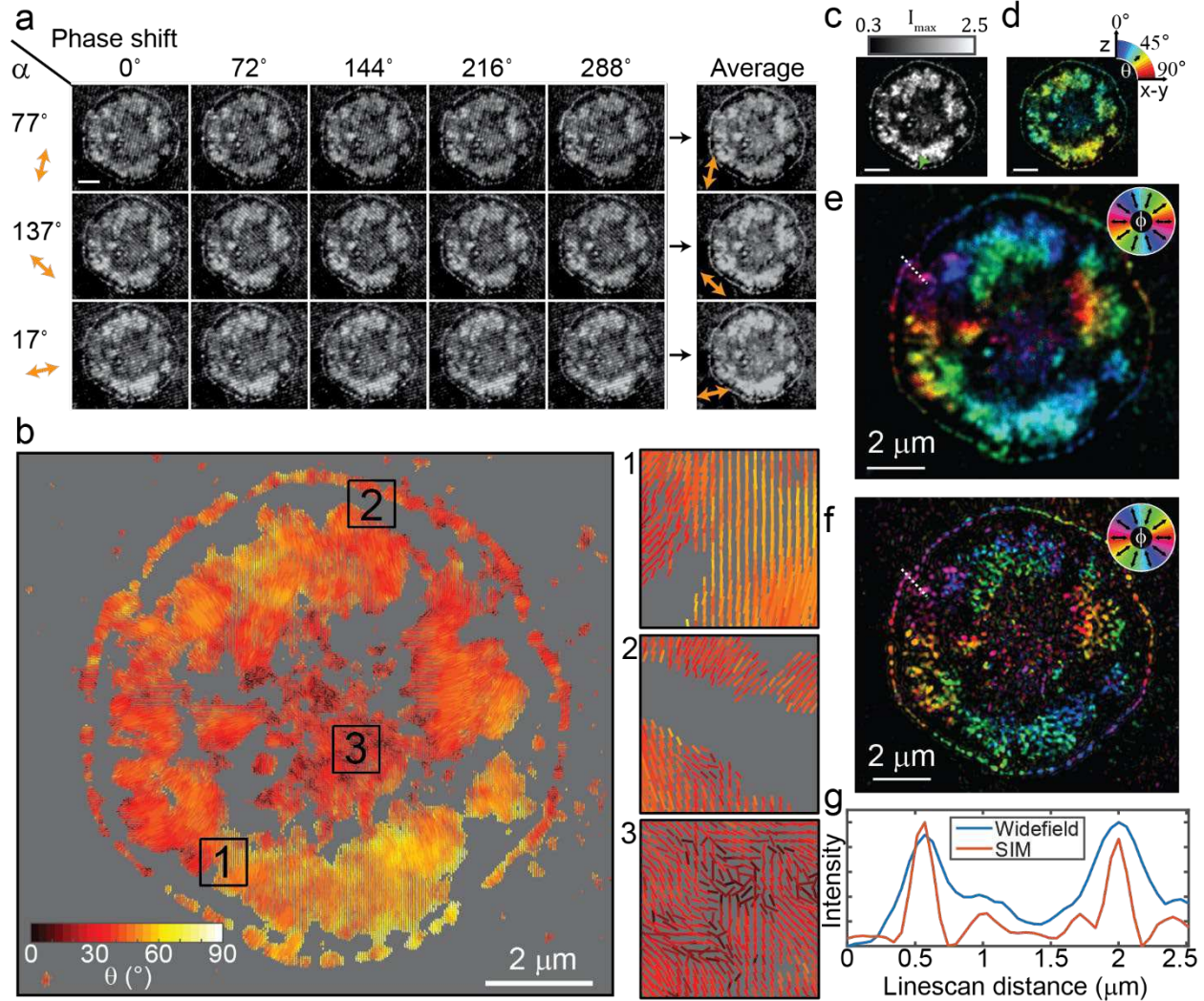


Figure 2: MFM can be performed on an unmodified SIM microscopy. **a)** Representative raw images of a platelet imaged using SIM-MFM. Fifteen images – one at each of 5 phase shifts and 3 illumination pattern orientations – are shown. The sinusoidal diffraction pattern can be seen upon careful inspection. Scale bar is $2 \mu m$. Images were contrast enhanced to make the striping pattern more apparent. **B)** Dipole orientation map of the platelet, wherein each pixel with I_{max} greater than a threshold (in this case, the 60% quantile of the image) has a dipole associated with it. For each dipole, ϕ is encoded in the dipole's orientation, θ is encoded in the dipole's color, and I_{max} is encoded in the dipole's length. Insets 1-3 show zoom-ins on specific regions of the dipole map. This display method was developed in our previous work. **C-e)** Alternative colormap-based display style used in this work showing **c)** I_{max} , **d)** θ , and **e)** ϕ for each pixel.

For *d* and *e*, the color reflects the measured force orientation. For all three colormaps, the brightness of each pixel is scaled to the I_{max} value shown in **c** (scale bar is $2 \mu m$). The images were also contrast adjusted such that the brightness is bounded to the 35th and 99th percentiles of the pixels' I_{max} values. **F**) Super-resolution reconstruction of the platelet. **G**) A linescan of the platelet's lamellipodial edge for both widefield (**c-e**) and super-resolution (**f**), showing an enhancement in spatial resolution when using the SIM reconstruction.

We utilized two rendering methods for displaying orientation data, both of which are shown in **Fig. 2**. Our first display method simultaneously shows I_{max} , ϕ , and θ . We mask the image to the 60th percentile intensity of the image and, for each pixel, plot a dipole (on a grey background) with orientation related to ϕ , length proportional to I_{max} , and color related to θ (**Fig. 2b**) (a percentile in this work refers to the intensity level that is brighter than that percent of pixels in the image). Our second display method is a colormap-based approach that gains some spatial detail at the expense of only being able to encode θ or ϕ in a single image⁴⁴. In this display method, orientation is linked to pixel color (using the circular HSV colormap for ϕ or the jet colormap for θ) and pixel brightness is linked to I_{max} (**Figs. 2c-e**, and **S2**). For clarity, we scaled the minimum and maximum pixel brightness to the 35th and 99th percentiles, respectively, of the entire image.

The platelets that we imaged with SIM-MFM displayed many characteristics that we observed in our original MFM study¹⁶. The platelets display two distinct regions of tension; at the lamellipodial edge and the inner lobe(s). As previously observed, the lamellipodial edges generally display a highly isotropic radial pattern (i.e. ϕ values are generally perpendicular to the platelet's edge and point towards the centroid of the platelet) while the platelets' inner regions generally display (with a few exceptions) two to four "lobes" that appear to act as independent and internally-homogenous mechanical units. For example, **Fig. S3** shows a platelet with two lobes in its inner region and a clearly visible lamellipodial edge. While the outer ring of lamellipodial tension points isotropically inward, the inner lobes display highly anisotropic contraction, with all dipoles within the lobes generally pointing to the central axis that bisects them. SIM-MFM also faithfully recapitulates previously-recorded θ values; an analysis of θ values across many platelets ($n = 37$ platelets) also revealed that the average θ value, $\langle\theta\rangle$, is $47 \pm 3^\circ$ which is similar to the value of $39 \pm 2^\circ$ that we measured previously¹⁶ and the $\sim 50 - 60^\circ$ measurement of the tilt angle of the adaptor protein talin^{27,55}.

We next used SIM-MFM to image integrin force orientation in a 3T3 mouse fibroblast cell line. Integrin forces in this cell line are primarily localized to focal adhesions (FAs), which are 100s of nm up to

many microns in size and apply force radially inward toward the center of the cell¹⁶. Our results using the SIM system reproduced these previous findings with the force orientation in FAs pointing toward the center of the cells (**Fig. 3**). **Figs. 3a** and **3b** show ϕ -colored diffraction limited and super-resolution maps, respectively, while a θ -colored map (**Fig. 3c**) shows tilt angles close to 45° , as shown previously¹⁶. We imaged 3T3 cells stably transfected with GFP-tagged Paxillin, a FA protein that generally colocalizes with integrin tension. Super-resolution reconstruction of the GFP-Paxillin image demonstrates an added benefit using the SIM-MFM approach: that nanoscale molecular organization and molecular force orientation and organization can be mapped in super-resolution concurrently with high temporal resolution (**Fig. 3d**). The super-resolution reconstructions of these images revealed that many regions of tension that would have been viewed as individual FA structures with MFM are in fact composed of multiple sub-micron traction structures with distinct mechanics (**Fig. 3e**).

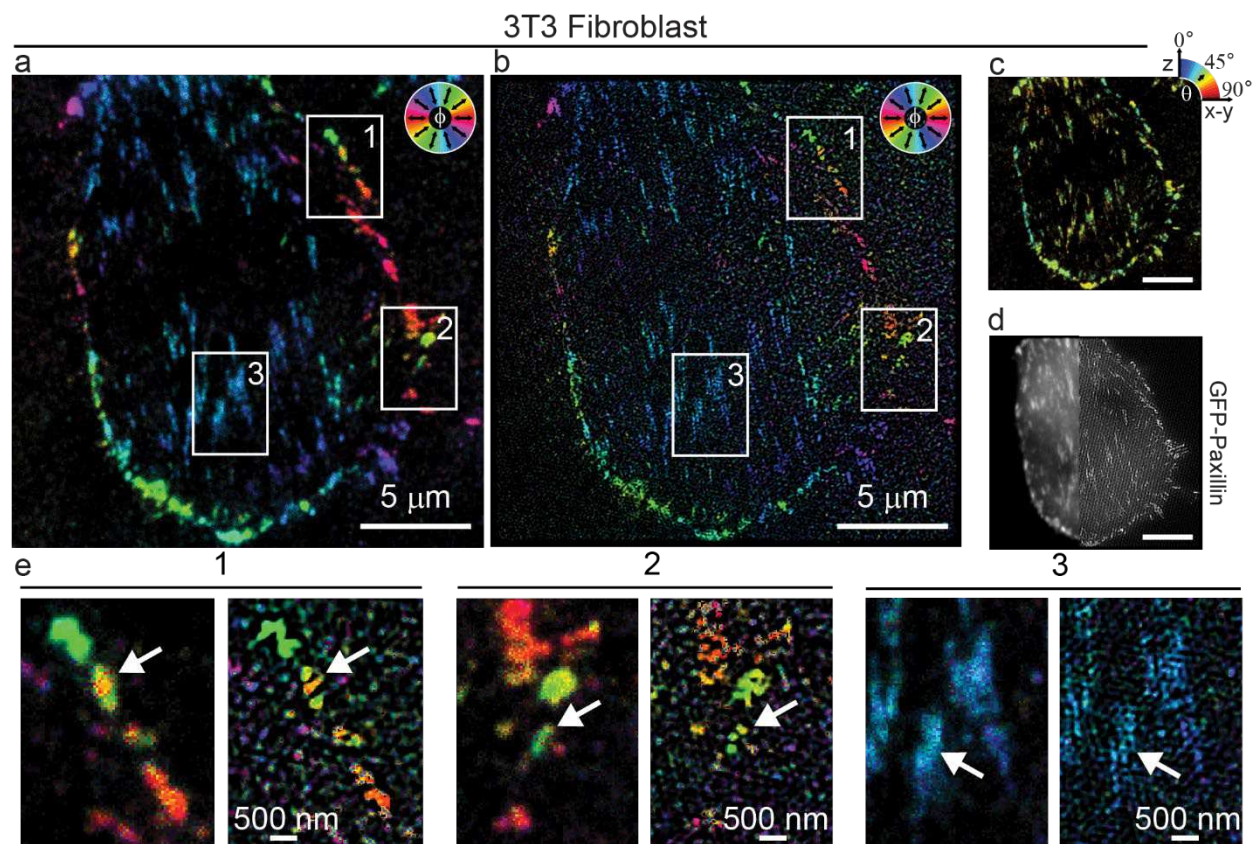


Figure 3: Representative 3T3 fibroblast data. **a-c)** Colormap-based display of orientation of integrin forces applied by an NIH 3T3 mouse fibroblast cell. ϕ -colored fluorescence images in **a)** widefield and **b)** super-resolution, as well as a **c)** widefield θ -colored image, are shown. **d)** GFP-tagged paxillin (an FA protein) is shown in widefield and super-resolution. **e)** Three zoom-ins denoted in **a)** and **b)** show FA structures (some denoted using white arrows) that can be resolved using super-resolution SIM-MFM that would otherwise appear to be blurred together using widefield MFM. Scale bars are $5 \mu m$ for full-cell images, 500 nm for zoom-in images.

Analysis of force orientation measurement error

We were initially concerned that the use of only 3 α angles (compared to 73, as previously used¹⁶) could potentially lead to systematic errors in θ and ϕ measurements due to inconsistencies in the effect of measurement noise on different force orientations. To examine this effect, we performed two validations. First, we conducted Monte Carlo simulations to evaluate the effect of true ϕ , θ , and I_{max} values on the accuracy (systematic and random error) of ϕ and θ measurements (**Fig. 4a, S4, S5** – see methods). Our results at the experimentally relevant signal level of $I_{max} = 1,000$ photons displayed small systematic errors in ϕ (less than half a degree across all orientations). As we observed in previous work¹⁶, random error in ϕ was high at low θ , and systematic error in θ was high at very low and high θ . Importantly, we did not observe a substantial dependence in any form of error on ϕ . While ε_ϕ , σ_ϕ , ε_θ , and σ_θ all exhibited slight periodic variations with respect to ϕ , these variations were all smaller than 1° . This was also true at a range of I_{max} from 100 photons to 10,000 photons (**Fig. S4-5**). These simulation results suggest that the use of only three α values introduces small ϕ -dependent orientation measurement errors.

To test this prediction, we plotted a histogram of ϕ values from 81 different platelets (**Fig. 4b**). Because all platelets are individually organized, all ϕ values should be measured with equal probability, resulting in a flat histogram. However, consistent with the simulation predictions we observed slight systematic biases that resulted in a non-flat histogram with local minima close to $\phi = 17^\circ$, 77° , and 137° . This small systematic error resulted in at most a 7% deviation from the ideal, and thus we do not expect this form of error to meaningfully bias our measurements.

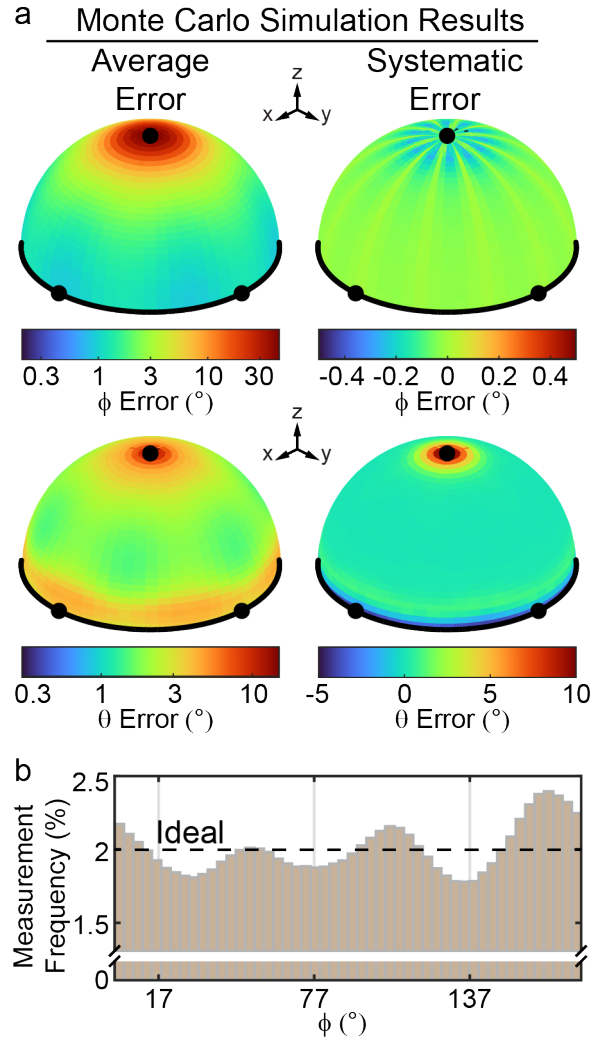


Fig. 4 Analysis of measurement errors. **a)** Results of Monte Carlo simulations of force orientation measurement. Four unit hemispheres are shown. The color of each point on a hemisphere denotes the error of the orientation that passes through that point. Average error (left) and systematic error (right) are shown for ϕ (top) and θ (bottom). **b)** Histogram of all ϕ values accumulated from 81 platelet timelapses. Dashed line shows the ideal behavior (2% measurement frequency in each of 50 bins). Small variations (from 1.81% to 2.16%) reveal a small effect of systematic errors. Only the brightest 50% of pixels were included in the analysis.

As a second means of investigating potential sources of systematic error in orientation measurement, we evaluated the ϕ dependence of θ measurements. To accomplish this, we assembled data from several platelets and calculated $\langle\theta\rangle$ values as a function of ϕ (**Fig. S6**). Ideally, $\langle\theta\rangle$ should not depend on ϕ in the compiled dataset. We found that $\langle\theta\rangle$ was constrained to a narrow range of $\sim 43 - 50^\circ$. The small scale of this variation ($\sim 7^\circ$) serves as a validation for SIM-MFM-based orientation measurement. However, ideally this variation would be on the order of $< 1^\circ$. This result, as well as the slight discrepancy between the $\langle\theta\rangle$ measured here and previously¹⁶ suggest that there may be slight measurement errors that were not fully corrected for in image pre-processing (e.g. variations in the illumination profile of the microscope).

Time-lapse imaging of platelets force alignment

SIM-MFM is a versatile technique that can be implemented in dynamic, living cells without substantial loss of signal due to photobleaching. We took advantage of this feature to investigate the dynamics of platelet spreading and adhesion. Our analysis, described below, reveals that, under our experimental conditions, platelet traction force aligns over time in a manner that can only be resolved using MFM. We added platelets to the solution over a tension probe-functionalized surface and imaged several locations on the surface at 2-minute intervals for 82 minutes. Over the course of this acquisition, we identified 81 platelets interacting with the surface. For each of these platelets, we segmented a small region-of-interest containing the platelet out of the imagestack (**Fig. 5a**). For each timepoint, we quantified the “tension area” (T), which is the surface area of the tension signal created by the platelet (**Fig. S7**), and a measure that we call the “alignment parameter” (**Fig. 5b, S8**). The alignment parameter, R , is a measure for the dispersion of all ϕ angles measured under a platelet. If all ϕ angles are aligned perfectly along the same axis, $R = 1$. If ϕ angles have an isotropic orientation, $R = 0$. In the context of directional statistics, the alignment parameter is equal to one minus the circular variance of the ϕ angles⁵⁶.

We found that tension area spiked sharply, quickly plateaued within a few minutes, then gradually or sharply dropped to zero within 10-30 minutes. We found that the T vs. time, t , curve for almost every platelet could be accurately described by the equation:

$$T \approx T_{max}u(t - t_{attach}) \left(\left(1 - \exp\left(-\frac{t - t_{attach}}{\tau_{spread}}\right) \right) - \left(\frac{1}{1 + \exp\left(-\frac{t - t_{attach} - t_{detach}}{\tau_{retract}}\right)} \right) \right) + T_0 \quad (8)$$

where T_{max} is the maximum tension area of the platelet, t_{attach} approximates the times at which the platelet attaches to the surface, t_{detach} approximates the duration between platelet adhesion and detachment, τ_{spread} and $\tau_{retract}$ are time constants for platelet spreading and retraction, respectively, T_0 is the basal T value measured (typically a noise-induced artifact) and $u(t - t_{attach})$ is the unit step function that denotes initiation of spreading at $t = t_{attach}$ (**Fig. 5b,c**). We set T_{max} , t_{attach} , t_{detach} , $\tau_{retract}$, and τ_{spread} all as fit parameters and used simulated annealing to fit eqn. (8) to each platelet's T vs. t data. We found that $T_{max} = 20 \pm 7 \mu m^2$ (median \pm inter-quartile range), and 46 had best-fit t_{attach} and t_{detach} values that fell within the duration of the imaging acquisition.

Of the 46 platelets in which the full process of attachment, spreading, retraction, and detachment was recorded, we quantified alignment, R , from t_{attach} to $t_{attach} + t_{detach}$. We found that roughly half ($N = 16$, 32%) exhibited no significant correlation between R and t (**Fig. 5d**). Of the remainder, alignment decreased over time for 6 (12%) and 28 (56%) exhibited a gradual, asymptotic increase in alignment (**Fig. 5e, S9**) that could generally be fit to the relationship:

$$R \approx R_{max} - (R_{max} - R_0) \exp\left(-\frac{t - t_{attach}}{\tau_{align}}\right) \quad (9)$$

where $R_0 = R_{min}$ and R_{max} are the minimum and maximum alignment parameters, and τ_{align} is the time constant for force alignment (only R_{max} , R_0 , and τ_{align} were set as fit parameters; t_{attach} from the T vs. t fit was used as a fixed parameter) (**Fig. 5b,c**). We split these cells into two groups (28 increasing alignment

cells and 22 cells with non-increasing alignment) and compared the sets of fit-parameters. While the 22 increasing-alignment platelets exhibited significantly different R_0 , and R_{max} values than the 28 cells with non-increasing R ($p < 0.001$, Wilcoxon rank-sum test), the dynamics of spreading were the same between the two groups ($p > 0.05$ for τ_{spread} , $\tau_{retract}$, and t_{detach}) (**Fig. 5f,g**).

We tested whether photobleaching may contribute to the apparent increase in alignment. Specifically, photobleaching could cause certain regions of tension to drop out of the R calculation, resulting in an artificially-increased R after several consecutive SIM-MFM acquisitions. To evaluate this possibility, we simulated photobleaching by taking the timepoint of maximum area for each of the 22 increasing-alignment timelapses and re-measured R and T while gradually decreasing I_{avg} for the entire image (**Fig. S10a**). As expected, substantial levels of simulated photobleaching did artificially increase R , generally by $\sim 25\%$ (**Fig. S10b**). However, we found that this source of error should produce a significant negative correlation between R and T (**Fig. S10c** – Pearson’s correlation coefficient = -0.38 , $p < 0.001$), and we observed no such correlation in the experimental results with the same set of platelets (**Fig. S10d**, $p = 0.07$). Moreover, we conducted an analysis of photobleaching that suggests that 30 minutes of imaging (15 SIM-MFM acquisitions taken at 2-min intervals) should result in $\sim 20\text{-}30\%$ photobleaching and only cause $\sim 15\%$ of pixels to drop out of the automated analysis (**Fig. S11**). Based on our simulated photobleaching results, these small effects are not expected to cause substantial changes in the measured alignment parameter (**Fig. S10**). Taken together, these analyses suggest that, while photobleaching could partly contribute to the increase in R observed, the effect of photobleaching is modest at best and increasing alignment is driven predominantly by the platelets’ phenotype as observed by integrin mechanics.

An interesting finding of this analysis is that spreading occurs on a significantly faster timescale than alignment; $\tau_{spread} = 1.7 \text{ min}$, while $\tau_{align} = 5.0 \text{ min}$ ($p < 0.001$, Wilcoxon rank-sum test) (**Fig. 5g**). This result suggests that platelet activation displays a characteristic mechanical progression that includes three phases. In the first phase, the platelet spreading area and the traction forces grow until reaching a steady state plateau. In the second phase, forces within the platelet re-organize and realign along

an axis. Finally, the platelet abruptly terminates contractility and detaches from the surface. We previously only quantified tension signal but not force orientation during platelet timelapse imaging^{4,57}, and so the second phase appeared to exhibit a constant net traction force magnitude.

We and others previously observed alignment of platelet contractile forces along an axis (or three or more axes all pointing inward) via MFM¹⁶, TFM^{51,58}, DNA tension gauge tether studies with complementary imaging of focal adhesion protein vinculin⁵², and super-resolution and electron microscopy of cytoskeletal filaments and vinculin⁵⁹. However, our work here represents, to the best of our knowledge, the first observation of alignment as a dynamic process, raising questions about the biophysical mechanisms underpinning this phenomenon. Previous atomic force microscopy (AFM) or TFM-type studies of single platelets pulling on deformable substrates have shown a gradual increase in single platelet forces over tens of minutes^{58,60,61}, but in our MTFM work we generally observe that the total tension signal plateaus after spreading and then eventually decreases^{4,57}. The similarity between the timescale of alignment observed in this work and the timescale of contraction observed using AFM/TFM suggests that alignment may be a means through which platelets increase the efficiency of contraction; if all integrin forces are aligned along a common axis, the bulk effect on the underlying surface will be greater than if the integrins are poorly aligned – even if the summed magnitude of tension applied through all integrins is the same in both scenarios. While the potential physiological relevance and biophysical underpinnings of these findings will require further investigation, alignment of platelet tension has been shown to depend on shear flow⁶², competent integrin signalling^{52,59}, and substrate stiffness⁵⁹. Proper alignment was also shown to be disrupted in a patient with Glanzmann thrombasthenia⁵⁹, wherein integrin signaling is dysregulated. Together, these studies have shown that integrin signaling is an important component in the process of alignment of platelet traction and the cytoskeleton, making SIM-MFM an ideal tool for the continued study of platelet mechanics.

Notably, a previous TFM-based study of platelet tension found that mild alignment established immediately upon platelet spreading and subsequently remained constant⁵⁸ (e.g., the first and third phases described above occur coincidentally). However, the discrepancy between that study and our results may

have resulted from a difference in substrate stiffness (a recent super-resolution study of actin organization showed that alignment of the actin cytoskeleton along an axis was more prominent on stiffer substrates⁵⁹), the lower spatial resolution of TFM, or differences in the identity and/or surface density of our ligands.

Table 1: Timelapse fit parameters for platelet spreading and tension alignment: Median (Inter-quartile range) with Wilcoxon rank-sum test p-values

	T_{max} (μm^2)	τ_{spread} (min)	$\tau_{retract}$ (min)	t_{detach} (min)	ΔR	R_{max}	τ_{align} (min)
Increasing alignment platelets (N=28)	18.2 (11.7, 26.6)	1.7 (0.1, 3.1)	5.0 (4.1, 8.3)	19.9 (16.4, 30.0)	0.38 (0.22, 0.54)	0.65 (0.43,0.78)	5.0 (3.3, 8.5)
Non-increasing alignment platelets (N=22)	17.6 (10.9, 23.1)	1.6 (0.6, 2.9)	4.1 (2.4, 12.8)	21.5 (10.9, 29.2)	0.28 (-0.14, 0.52)	0.61 (0.21, 0.74)	-
p-value	0.56	0.93	0.99	0.79	0.30	0.28	-

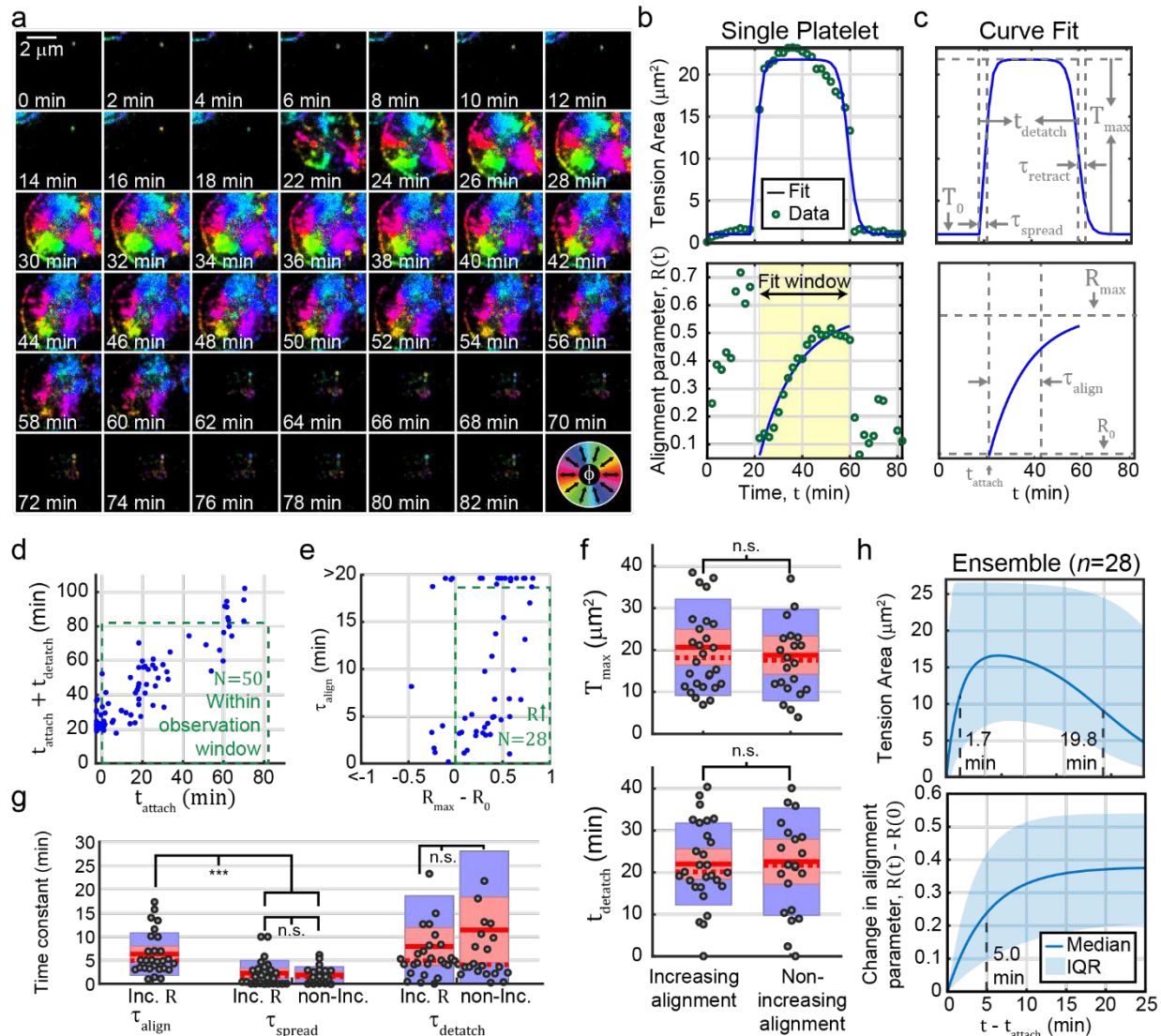


Fig. 5: Dynamic properties of human platelets revealed using SIM-MFM. **a)** Timelapse of a platelet spreading on a surface, shown using the ϕ -colormap display method (see color wheel in bottom right corner). Gradual tension alignment can be seen via careful inspection; greens and cyans are common at early timepoints, but gradually transition to purple and dark blue due to alignment of platelet tension. **b)** Tension area (top) and the alignment parameter, R , quantified as a function of time, t , with curve fits shown (blue). Yellow shading denotes time window of platelet attachment. **c)** Best-fit curves from **b)** with annotations depicting fit parameters. **d)** scatterplot of best-fit $t_{attach} + t_{detach}$ (the timepoint at which platelet detachment occurs) and t_{attach} (the timepoint at which attachment occurs)

values. Green dashed line shows the parameter space in which attachment and detachment both occurred within the duration of the timelapse. **e)** Scatterplot of best-fit τ_{align} (the time constant for tension alignment) and ΔR (the change in alignment) values for the platelets selected from **d**. Green line shows selected population with increasing alignment. **f)** Boxplots of T_{max} (the max platelet spread area – top) and t_{detach} (the duration of platelet attachment – bottom) for the 28 cells selected in **e**. Solid red line indicates mean, dashed red line indicates median, red boxes show standard error of the mean and blue boxes shows 95% confidence interval of the mean. Grey circles indicate individual datapoints. **g)** Boxplots for τ_{align} , τ_{spread} (the time constant for platelet spreading), and τ_{detach} (the time constant for platelet retraction). *** denotes $p < 0.001$, and n.s. denotes $p > 0.05$ (Wilcoxon rank-sum test for difference in population medians). **h)** Depiction of ensemble behavior. Blue curves denote reconstruction with median best-fit parameters and blue shading denote range of values obtained using all possible combinations of 25th, 50th, and 75th percentile best-fit parameters.

SIM-MFM measurement of T-cell receptor forces

As a final experiment in our proof-of-concept SIM-MFM study, we investigated the anisotropic mechanosensor hypothesis of T-cell receptor (TCR) activation³. Previous work suggested that application of lateral tension to the TCR is more likely to stimulate an immune response compared to force that is applied perpendicular to the plasma membrane³. In that work, optical tweezers were used to apply tension to T-cells. While this single molecule experiment provides insights into the potential role of force orientation on TCR triggering, in physiological settings the TCR itself couples to the cytoskeleton and transmits forces that are resisted by the pMHC ligand on the apposed cell membrane. SIM-MFM offers an opportunity to measure the orientation of forces applied directly by a T-cell's own cytoskeletal activity. The observation of lateral forces applied by the TCR would support the anisotropic mechanosensor model.

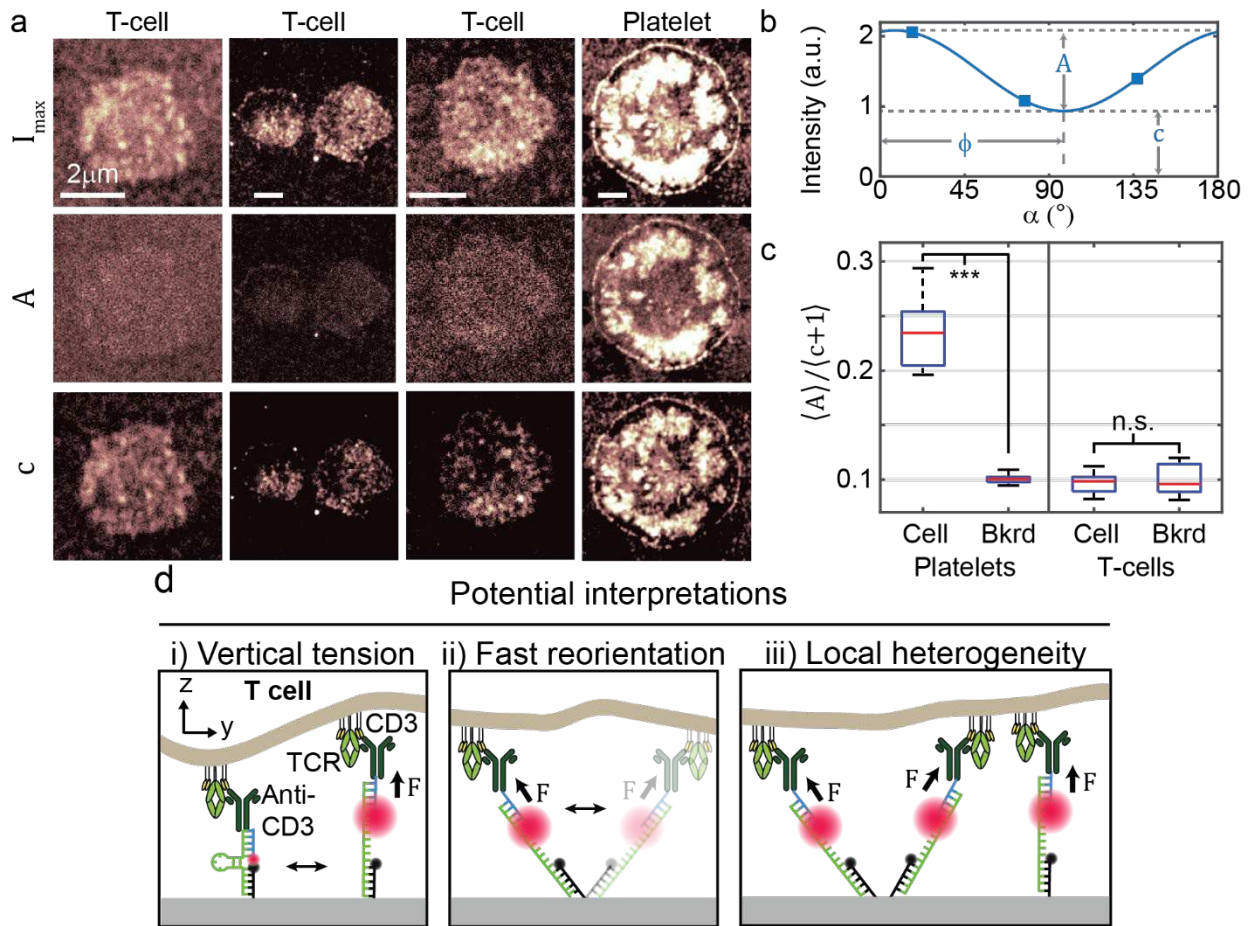


Fig. 6: Analysis of T-cell receptor tension reveals no polarization-dependence

a) Three example T-cells and one platelet are shown in three panels each. The top row shows I_{max} , the second row shows the polarization-dependent component of the fit sinusoid, A , and the third row shows the polarization independent component of the fit sinusoid, c . While platelets display substantial polarization dependence (high A), T-cells exhibit almost no polarization dependence (low A)

b) A fit sinusoid is shown with A and c depicted (adapted from Fig. 1c). **c)** A quantification of the polarization response, $\langle A \rangle / (\langle c \rangle + 1)$ (the averaged polarization-dependent component divided by the average polarization-independent component of the fit sinusoids) of several ($N > 25$) T-cells and platelets, both under the cell and in the surrounding background close to the cell. While platelets exhibit a much higher polarization response than the background signal, T-cells do not. **d)** Three potential causes of the

lack of polarization response in T-cells. TCR forces may be some combination of i) vertical to the glass surface, ii) highly dynamic such that the orientation of each open tension probe is randomized during the ~100 ms exposure time of each image, and iii) locally heterogenous such that neighboring probes obfuscate eachothers' polarization responses. All three of these scenarios can result in the lack of polarization response observed.

We cultured primary mouse CD8+ T-cells on DNA hairpin tension probes that present antibodies to CD3 ϵ (CD3 ϵ is part of the TCR complex which includes CD3 δ , γ and ζ chains, as well as the TCR α/β chains). As observed previously^{17,63}, T-cells spread on the tension probe-functionalized surface, and the TCRs engaged and mechanically unfold tension probes to generate bright tension fluorescence signal. We imaged several cells (N=26 cells from 3 independent surface) and were surprised to find that T-cells did not exhibit any notable polarization-dependent response (**Figs. 6, S12**). Our results, discussed in greater detail in **Supplemental Note 2**, suggest that TCR force vectors lack a detectable lateral organization at the \sim 100 nm length scale. This is in stark contrast to traction forces generated by platelets and fibroblasts. This result can be due to a combination of three main factors. First, TCR forces may be perpendicular to the substrate. This is unlikely given that the T-cell membrane displays TCR loaded projections including microvilli^{64,65}. Such structures are unlikely to uniformly pull in the vertical direction. Second, tension probes may undergo fast reorientation, wherein individual open tension probes rapidly reorient within the timescale of an individual image. Third, TCR forces may be highly heterogeneous (at the sub-100 nm length scale). These last two scenarios would be surprising as frictional coupling between TCRs and actin flow is believed to generate TCR forces and actin flow are generally persistent at the micrometer length scale for timescales much longer than individual acquisitions. These results neither support nor refute the anisotropic mechanosensor hypothesis, which was tested by applying external forces to T-cells rather than measuring their intrinsically-applied forces³. Instead, our findings show that if lateral forces are indeed a potent trigger signal for TCR activation, then these forces will be difficult to image as they are likely to be disorganized and/or highly transient. Accordingly, there is a need for further development in this area to simultaneously capture TCR force orientation and TCR triggering with molecular resolution, potentially by combining SIM-MFM with techniques for single molecule visualization of cell-generated forces^{18,66}.

Discussion

We have demonstrated that a SIM microscope can be used to implement MFM for rapid mapping of molecular force orientation at \sim 100 nm resolution. To demonstrate the broad applicability of this

technique, we used SIM-MFM to image platelets, fibroblasts, and T-cells. We have shown that the resolution enhancement afforded by SIM can reveal traction structures that are not resolvable with conventional widefield imaging methods. While this resolution enhancement could in theory be accomplished by applying computational approaches to conventional MFM datasets⁶⁷, the SIM-MFM approach has the added benefit of enabling MFM using commercially-available SIM microscopes in a turn-key fashion. SIM-MFM also enables rapid super-resolution imaging of structural proteins such as paxillin in parallel with super-resolution imaging of force magnitude and orientation, and facile, photostable timelapse imaging of molecular force orientation. We expect that ongoing SIM and pSIM technique developments will continue to improve SIM-MFM acquisition⁶⁸⁻⁷⁰. Perhaps eventually, SIM will be performed with E dipoles that are not parallel to the coverslip, which would enable nondegenerate force vector mapping⁴⁰.

In our proof-of-concept studies, we have demonstrated that platelets undergo traction force realignment on a timescale that is substantially longer than the timescale of platelet spreading (7 min vs. 1.7 min, respectively). We have also shown that TCR forces are, in contrast to the integrin traction forces that we generally study with MFM, not temporally stable, homogeneously aligned, and lateral. We expect that SIM-MFM will be used in several future applications in cellular biology and for the investigation of force generation by active nanomaterials, which is an emerging application area of DNA mechanotechnology tension probes^{71,72}.

Methods

Materials and methods can be found in the supplementary information file.

Acknowledgements

We thank Laura Fox-Goharioon, Neil Anthony, and William Giang of the Integrated Cellular Imaging Core at Emory University for maintaining and troubleshooting the SIM microscope used in this work. We

also thank Tejeshwar Rao, Reena Beggs, Tomasz Nawara, and Will Dean of the Mattheyses lab at UAB for helpful conversations.

References

- 1 Chen, Y., Ju, L., Rushdi, M., Ge, C. & Zhu, C. Receptor-mediated cell mechanosensing. *Mol. Biol. Cell* **28**, 3134-3155, doi:10.1091/mbc.E17-04-0228 (2017).
- 2 Jansen, K. A. *et al.* A guide to mechanobiology: Where biology and physics meet. *Biochim. Biophys. Acta* **1853**, 3043-3052, doi:<https://doi.org/10.1016/j.bbamcr.2015.05.007> (2015).
- 3 Kim, S. T. *et al.* The alphabeta T cell receptor is an anisotropic mechanosensor. *J. Biol. Chem.* **284**, 31028–31037, doi: 10.1074/jbc.M109.052712 (2009).
- 4 Zhang, Y. *et al.* Platelet integrins exhibit anisotropic mechanosensing and harness piconewton forces to mediate platelet aggregation. *Proc. Natl. Acad. Sci. U. S. A.*, doi:10.1073/pnas.1710828115 (2017).
- 5 Evans, E. A. & Calderwood, D. A. Forces and bond dynamics in cell adhesion. *Science* **316**, 1148-1153, doi:10.1126/science.1137592 (2007).
- 6 Levental, K. R. *et al.* Matrix crosslinking forces tumor progression by enhancing integrin signaling. *Cell* **139**, 891-906, doi:10.1016/j.cell.2009.10.027 (2009).
- 7 Qiu, Y. *et al.* Platelet mechanosensing of substrate stiffness during clot formation mediates adhesion, spreading, and activation. *Proc. Natl. Acad. Sci. U. S. A.* **111**, 14430-14435, doi:10.1073/pnas.1322917111 (2014).
- 8 Zhang, Y., Ge, C., Zhu, C. & Salaita, K. DNA-based digital tension probes reveal integrin forces during early cell adhesion. *Nat Commun* **5**, 5167, doi:10.1038/ncomms6167 (2014).
- 9 Liu, Y., Yehl, K., Narui, Y. & Salaita, K. Tension Sensing Nanoparticles for Mechano-Imaging at the Living/Nonliving Interface. *J. Am. Chem. Soc.* **135**, 5320-5323, doi:10.1021/ja401494e (2013).
- 10 Stabley, D. R., Jurchenko, C., Marshall, S. S. & Salaita, K. S. Visualizing mechanical tension across membrane receptors with a fluorescent sensor. *Nat. Methods* **9**, 64-67, doi:10.1038/nmeth.1747 (2011).
- 11 Chang, Y. *et al.* A General Approach for Generating Fluorescent Probes to Visualize Piconewton Forces at the Cell Surface. *J. Am. Chem. Soc.* **138**, 2901-2904, doi:10.1021/jacs.5b11602 (2016).
- 12 Jurchenko, C., Chang, Y., Narui, Y., Zhang, Y. & Salaita, Khalid S. Integrin-Generated Forces Lead to Streptavidin-Biotin Unbinding in Cellular Adhesions. *Biophys. J.* **106**, 1436-1446, doi:10.1016/j.bpj.2014.01.049 (2014).
- 13 Ma, V. P.-Y. *et al.* Ratiometric tension probes for mapping receptor forces and clustering at intermembrane junctions. *Nano Lett.* **16**, 4552–4559, doi:10.1021/acs.nanolett.6b01817 (2016).
- 14 Blakely, B. L. *et al.* A DNA-based molecular probe for optically reporting cellular traction forces. *Nat. Methods* **11**, 1229-1232, doi:10.1038/nmeth.3145 (2014).
- 15 Ma, V. P.-Y. *et al.* The Mechanically-induced Catalytic Amplification Reaction for Readout of Receptor-Mediated Cellular Forces. *Angew. Chem. Int. Ed.* **55**, 5488-5492, doi:10.1002/anie.201600351 (2016).
- 16 Brockman, J. M. *et al.* Mapping the 3D orientation of piconewton integrin traction forces. *Nat. Methods* **15**, 115, doi:10.1038/nmeth.4536 (2017).
- 17 Liu, Y. *et al.* DNA-based nanoparticle tension sensors reveal that T-cell receptors transmit defined pN forces to their antigens for enhanced fidelity. *Proc. Natl. Acad. Sci. U. S. A.* **113**, 5610-5615, doi:10.1073/pnas.1600163113 (2016).
- 18 Brockman, J. M. *et al.* Live-cell super-resolved PAINT imaging of piconewton cellular traction forces. *Nat. Methods*, doi:10.1038/s41592-020-0929-2 (2020).

- 19 Kornelia, G. *et al.* Molecular Tension Probes to Investigate the Mechanopharmacology of Single Cells: A Step toward Personalized Mechanomedicine. *Advanced Healthcare Materials* **0**, 1800069, doi:doi:10.1002/adhm.201800069.
- 20 Galior, K., Liu, Y., Yehl, K., Vivek, S. & Salaita, K. Titin-Based Nanoparticle Tension Sensors Map High-Magnitude Integrin Forces within Focal Adhesions. *Nano Lett.* **16**, 341-348, doi:10.1021/acs.nanolett.5b03888 (2016).
- 21 Ma, V. P.-Y. *et al.* Ratiometric tension probes for mapping receptor forces and clustering at intermembrane junctions. *Nano Lett.*, doi:10.1021/acs.nanolett.6b01817 (2016).
- 22 Glazier, R. *et al.* DNA mechanotechnology reveals that integrin receptors apply pN forces in podosomes on fluid substrates. *Nat. Commun.* **10**, 4507, doi:10.1038/s41467-019-12304-4 (2019).
- 23 Kaganman, I. Unwinding to measure tension. *Nat. Methods* **11**, 1200-1200, doi:10.1038/nmeth.3202 (2014).
- 24 Polacheck, W. J. & Chen, C. S. Measuring cell-generated forces: a guide to the available tools. *Nat. Methods* **13**, 415-423, doi:10.1038/nmeth.3834 (2016).
- 25 Roca-Cusachs, P., Conte, V. & Trepats, X. Quantifying forces in cell biology. *Nat. Cell Biol.* **19**, 742-751, doi:10.1038/ncb3564 (2017).
- 26 Huang, D. L., Bax, N. A., Buckley, C. D., Weis, W. I. & Dunn, A. R. Vinculin forms a directionally asymmetric catch bond with F-actin. *Science* **357**, 703 (2017).
- 27 Kanchanawong, P. *et al.* Nanoscale architecture of integrin-based cell adhesions. *Nature* **468**, 580-585, doi:10.1038/nature09621 (2010).
- 28 Poulter, N. S. *et al.* Platelet actin nodules are podosome-like structures dependent on Wiskott–Aldrich syndrome protein and ARP2/3 complex. *Nat. Commun.* **6**, 7254, doi:10.1038/ncomms8254 (2015).
- 29 Blanchard, A. T. & Salaita, K. Emerging uses of DNA mechanical devices. *Science* **365**, 1080-1081, doi:10.1126/science.aax3343 (2019).
- 30 DeMay, Bradley S., Noda, N., Gladfelter, Amy S. & Oldenbourg, R. Rapid and Quantitative Imaging of Excitation Polarized Fluorescence Reveals Ordered Septin Dynamics in Live Yeast. *Biophys. J.* **101**, 985-994, doi:10.1016/j.bpj.2011.07.008 (2011).
- 31 Bartle, E. I., Urner, T. M., Raju, S. S. & Mattheyses, A. L. Desmoglein 3 Order and Dynamics in Desmosomes Determined by Fluorescence Polarization Microscopy. *Biophys. J.* **113**, 2519-2529, doi:10.1016/j.bpj.2017.09.028 (2017).
- 32 Duboisset, J. *et al.* Thioflavine-T and Congo Red Reveal the Polymorphism of Insulin Amyloid Fibrils When Probed by Polarization-Resolved Fluorescence Microscopy. *J. Phys. Chem. B* **117**, 784-788, doi:10.1021/jp309528f (2013).
- 33 Timr, Š. *et al.* Accurate Determination of the Orientational Distribution of a Fluorescent Molecule in a Phospholipid Membrane. *J. Phys. Chem. B* **118**, 855-863, doi:10.1021/jp4067026 (2014).
- 34 Kress, A. *et al.* Mapping the Local Organization of Cell Membranes Using Excitation-Polarization-Resolved Confocal Fluorescence Microscopy. *Biophys. J.* **105**, 127-136, doi:<https://doi.org/10.1016/j.bpj.2013.05.043> (2013).
- 35 Abrahamsson, S. *et al.* MultiFocus Polarization Microscope (MF-PolScope) for 3D polarization imaging of up to 25 focal planes simultaneously. *Opt. Express* **23**, 7734-7754, doi:10.1364/OE.23.007734 (2015).
- 36 McQuilken, M. *et al.* Analysis of Septin Reorganization at Cytokinesis Using Polarized Fluorescence Microscopy. *Front. Cell Dev. Biol.* **5**, doi:10.3389/fcell.2017.00042 (2017).
- 37 Wang, X., Kress, A., Brasselet, S. & Ferrand, P. High frame-rate fluorescence confocal angle-resolved linear dichroism microscopy. *Rev. Sci. Instrum.* **84**, 053708, doi:10.1063/1.4807318 (2013).

- 38 Backer, A. S., Lee, M. Y. & Moerner, W. E. Enhanced DNA imaging using super-resolution microscopy and simultaneous single-molecule orientation measurements. *Optica* **3**, 659-666, doi:10.1364/OPTICA.3.000659 (2016).
- 39 Backer, A. S. *et al.* Single-molecule polarization microscopy of DNA intercalators sheds light on the structure of S-DNA. *Sci. Adv.* **5**, eaav1083, doi:10.1126/sciadv.aav1083 (2019).
- 40 Blanchard, A. T., Brockman, J. M., Salaita, K. & Mattheyses, A. L. Variable incidence angle linear dichroism (VALiD): a technique for unique 3D orientation measurement of fluorescent ensembles. *Opt. Express* **28**, 10039-10061, doi:10.1364/OE.381676 (2020).
- 41 Woodside, M. T. *et al.* Nanomechanical measurements of the sequence-dependent folding landscapes of single nucleic acid hairpins. *Proc. Natl. Acad. Sci. U. S. A.* **103**, 6190-6195, doi:10.1073/pnas.0511048103 (2006).
- 42 Iqbal, A., Wang, L., Thompson, K. C., Lilley, D. M. J. & Norman, D. G. The Structure of Cyanine 5 Terminally Attached to Double-Stranded DNA: Implications for FRET Studies. *Biochemistry* **47**, 7857-7862, doi:10.1021/bi800773f (2008).
- 43 Iqbal, A. *et al.* Orientation dependence in fluorescent energy transfer between Cy3 and Cy5 terminally attached to double-stranded nucleic acids. *Proc. Natl. Acad. Sci. U. S. A.* **105**, 11176, doi:10.1073/pnas.0801707105 (2008).
- 44 Zhanghao, K. *et al.* Super-resolution imaging of fluorescent dipoles via polarized structured illumination microscopy. *Nat. Commun.* **10**, 4694, doi:10.1038/s41467-019-12681-w (2019).
- 45 Gustafsson, M. G. L. Surpassing the lateral resolution limit by a factor of two using structured illumination microscopy. *J. Microsc.* **198**, 82-87, doi:10.1046/j.1365-2818.2000.00710.x (2000).
- 46 Gustafsson, M. G. L. *et al.* Three-Dimensional Resolution Doubling in Wide-Field Fluorescence Microscopy by Structured Illumination. *Biophys. J.* **94**, 4957-4970, doi:<https://doi.org/10.1529/biophysj.107.120345> (2008).
- 47 Schermelleh, L. *et al.* Subdiffraction Multicolor Imaging of the Nuclear Periphery with 3D Structured Illumination Microscopy. *Science* **320**, 1332, doi:10.1126/science.1156947 (2008).
- 48 York, A. G. *et al.* Resolution doubling in live, multicellular organisms via multifocal structured illumination microscopy. *Nat. Methods* **9**, 749-754, doi:10.1038/nmeth.2025 (2012).
- 49 Haubner, R. *et al.* Structural and Functional Aspects of RGD-Containing Cyclic Pentapeptides as Highly Potent and Selective Integrin $\alpha V\beta 3$ Antagonists. *J. Am. Chem. Soc.* **118**, 7461-7472, doi:10.1021/ja9603721 (1996).
- 50 Sachs, L., Denker, C., Greinacher, A. & Palankar, R. Quantifying single-platelet biomechanics: An outsider's guide to biophysical methods and recent advances. *Research and Practice in Thrombosis and Haemostasis* **4**, 386-401, doi:10.1002/rth2.12313 (2020).
- 51 Schwarz Henriques, S., Sandmann, R., Strate, A. & Koster, S. Force field evolution during human blood platelet activation. *J. Cell Sci.* **125**, 3914-3920, doi:10.1242/jcs.108126 (2012).
- 52 Wang, Y. *et al.* Force-activatable biosensor enables single platelet force mapping directly by fluorescence imaging. *Biosens. Bioelectron.* **100**, 192-200, doi:10.1016/j.bios.2017.09.007 (2018).
- 53 Style, R. W. *et al.* Traction force microscopy in physics and biology. *Soft Matter* **10**, 4047-4055, doi:10.1039/C4SM00264D (2014).
- 54 Müller, M., Mönkemöller, V., Hennig, S., Hübner, W. & Huser, T. Open-source image reconstruction of super-resolution structured illumination microscopy data in ImageJ. *Nat. Commun.* **7**, 10980, doi:10.1038/ncomms10980 (2016).
- 55 Paszek, M. J. *et al.* Scanning angle interference microscopy reveals cell dynamics at the nanoscale. *Nat. Methods* **9**, 825, doi:10.1038/nmeth.2077

<https://www.nature.com/articles/nmeth.2077#supplementary-information> (2012).

56 in *Directional Statistics* 13-24 (1999).

- 57 Dutta, P. K. *et al.* Programmable Multivalent DNA-Origami Tension Probes for Reporting Cellular Traction Forces. *Nano Lett.* **18**, 4803-4811, doi:10.1021/acs.nanolett.8b01374 (2018).
- 58 Hanke, J., Probst, D., Zemel, A., Schwarz, U. S. & Köster, S. Dynamics of force generation by spreading platelets. *Soft Matter* **14**, 6571-6581, doi:10.1039/c8sm00895g (2018).
- 59 Lickert, S. *et al.* Morphometric analysis of spread platelets identifies integrin $\alpha\text{IIb}\beta\text{3}$ -specific contractile phenotype. *Sci. Rep.* **8**, 5428, doi:10.1038/s41598-018-23684-w (2018).
- 60 Lam, W. A. *et al.* Mechanics and contraction dynamics of single platelets and implications for clot stiffening. *Nature Materials* **10**, 61-66, doi:10.1038/nmat2903 (2011).
- 61 Myers, D. R. *et al.* Single-platelet nanomechanics measured by high-throughput cytometry. *Nature Materials* **16**, 230-235, doi:10.1038/nmat4772 (2017).
- 62 Hanke, J., Ranke, C., Perego, E. & Köster, S. Human blood platelets contract in perpendicular direction to shear flow. *Soft Matter* **15**, 2009-2019, doi:10.1039/C8SM02136H (2019).
- 63 Ma, R. *et al.* DNA probes that store mechanical information reveal transient piconewton forces applied by T cells. *Proc. Natl. Acad. Sci. U. S. A.* **116**, 16949, doi:10.1073/pnas.1904034116 (2019).
- 64 Jung, Y. *et al.* Three-dimensional localization of T-cell receptors in relation to microvilli using a combination of superresolution microscopies. *Proc. Natl. Acad. Sci. U. S. A.* **113**, E5916, doi:10.1073/pnas.1605399113 (2016).
- 65 Kim, H.-R. *et al.* T cell microvilli constitute immunological synaptosomes that carry messages to antigen-presenting cells. *Nat. Commun.* **9**, 3630, doi:10.1038/s41467-018-06090-8 (2018).
- 66 Tan, S. J. *et al.* Regulation and dynamics of force transmission at individual cell-matrix adhesion bonds. *Sci. Adv.* **6**, eaax0317, doi:10.1126/sciadv.aax0317 (2020).
- 67 Zhanghao, K. *et al.* Super-resolution dipole orientation mapping via polarization demodulation. *Light: Science & Applications* **5**, e16166, doi:10.1038/lsa.2016.166
<https://www.nature.com/articles/lsa2016166#supplementary-information> (2016).
- 68 Chen, X. *et al.* Enhanced reconstruction of structured illumination microscopy on a polarized specimen. *Opt. Express* **28**, 25642-25654, doi:10.1364/OE.395092 (2020).
- 69 Jin, L. *et al.* Deep learning enables structured illumination microscopy with low light levels and enhanced speed. *Nat. Commun.* **11**, 1934, doi:10.1038/s41467-020-15784-x (2020).
- 70 Cnossen, J. *et al.* Localization microscopy at doubled precision with patterned illumination. *Nat. Methods* **17**, 59-63, doi:10.1038/s41592-019-0657-7 (2020).
- 71 Blanchard, A. T. *et al.* Highly polyvalent DNA motors generate 100+ piconewtons of force via autochemophoresis. *Nano Lett.*, doi:10.1021/acs.nanolett.9b02311 (2019).
- 72 Su, H. *et al.* Light-Responsive Polymer Particles as Force Clamps for the Mechanical Unfolding of Target Molecules. *Nano Lett.* **18**, 2630-2636, doi:10.1021/acs.nanolett.8b00459 (2018).

Figures

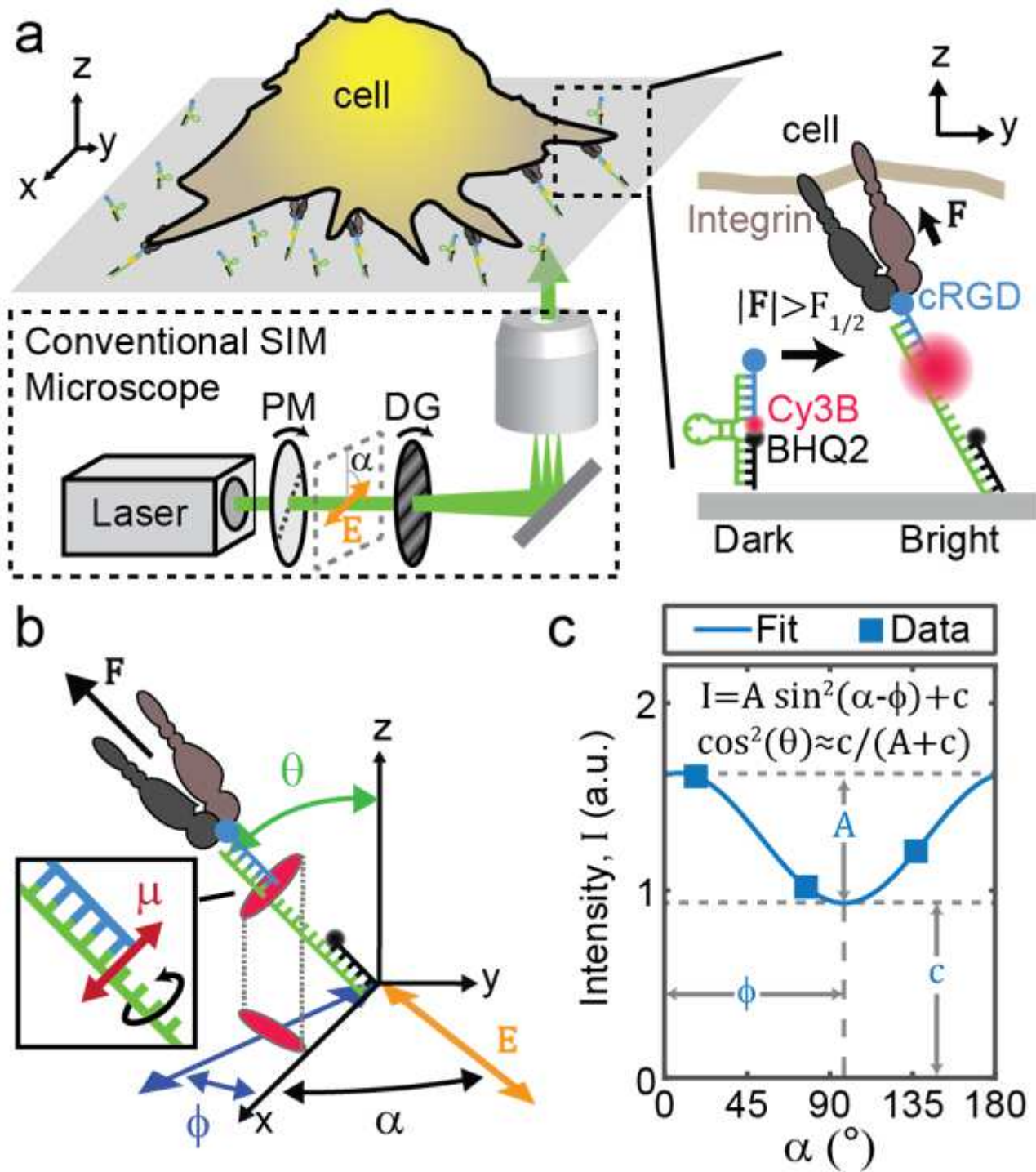


Figure 1

SIM-MFM concept a) Diagram showing microscope setup and DNA hairpin-based tension probe function. We show the basic components of a SIM microscope excitation line: a linearly-polarized laser passes through a polarization modulator (PM) and diffraction grating (DG). These two components rotate

together such that α (the angle of the laser beam's electric field vector, E) is the same as the orientation of the striping pattern created by the DG. Inset shows a DNA hairpin-based tension probe (blue, green, and black DNA strands) transitioning from a closed state to an opened state upon application of tension (F) with a magnitude exceeding the probe's $F_{(1/2)}$ value. Cell receptor (brown and gray) is an integrin and the ligand (blue circle) is cRGD. b) Illustration of F (black arrow) and E (orange dipole) angles used in this work. Inset shows Cy3b transition dipole moment (μ) perpendicular to the long axis of the tension probe. c) Representative data and curve fit from a pixel indicated in Fig. 2c (green arrow). A , c , and \bar{x} are illustrated and the equations used to obtain curve fit from data are shown.

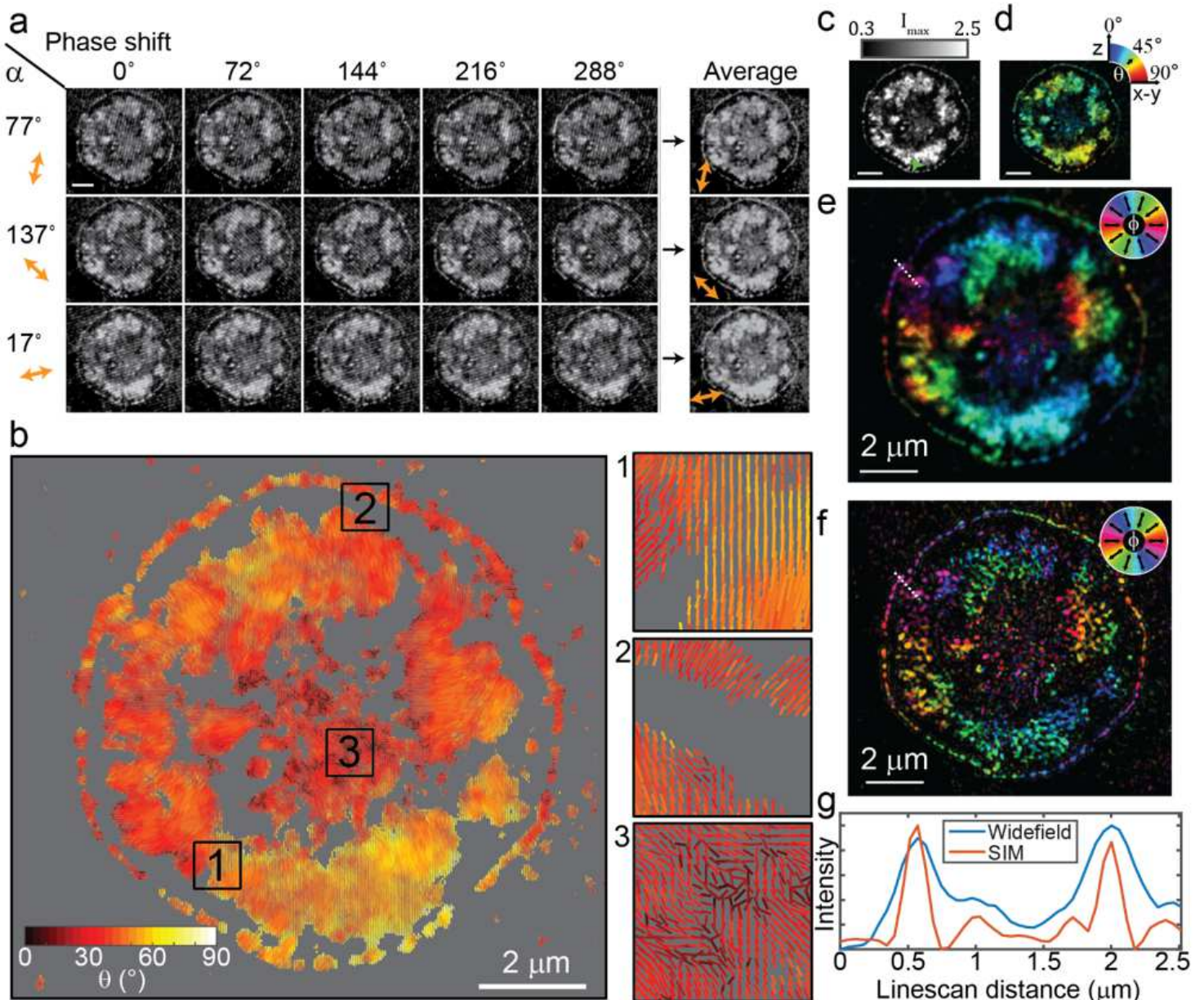


Figure 2

MFM can be performed on an unmodified SIM microscopy. a) Representative raw images of a platelet imaged using SIM-MFM. Fifteen images – one at each of 5 phase shifts and 3 illumination pattern orientations – are shown. The sinusoidal diffraction pattern can be seen upon careful inspection. Scale

bar is 2 μm . Images were contrast enhanced to make the striping pattern more apparent. B) Dipole orientation map of the platelet, wherein each pixel with I_{max} greater than a threshold (in this case, the 60% quantile of the image) has a dipole associated with it. For each dipole, ϕ is encoded in the dipole's orientation, θ is encoded in the dipole's color, and I_{max} is encoded in the dipole's length. Insets 1-3 show zoom-ins on specific regions of the dipole map. This display method was developed in our previous work. C-e) Alternative colormap-based display style used in this work showing c) I_{max} , d) θ , and e) ϕ for each pixel. For d and e, the color reflects the measured force orientation. For all three colormaps, the brightness of each pixel is scaled to the I_{max} value shown in c (scale bar is 2 μm). The images were also contrast adjusted such that the brightness is bounded to the 35th and 99th percentiles of the pixels' I_{max} values. F) Super-resolution reconstruction of the platelet. G) A linescan of the platelet's lamellipodial edge for both widefield (c-e) and super-resolution (f), showing an enhancement in spatial resolution when using the SIM reconstruction.

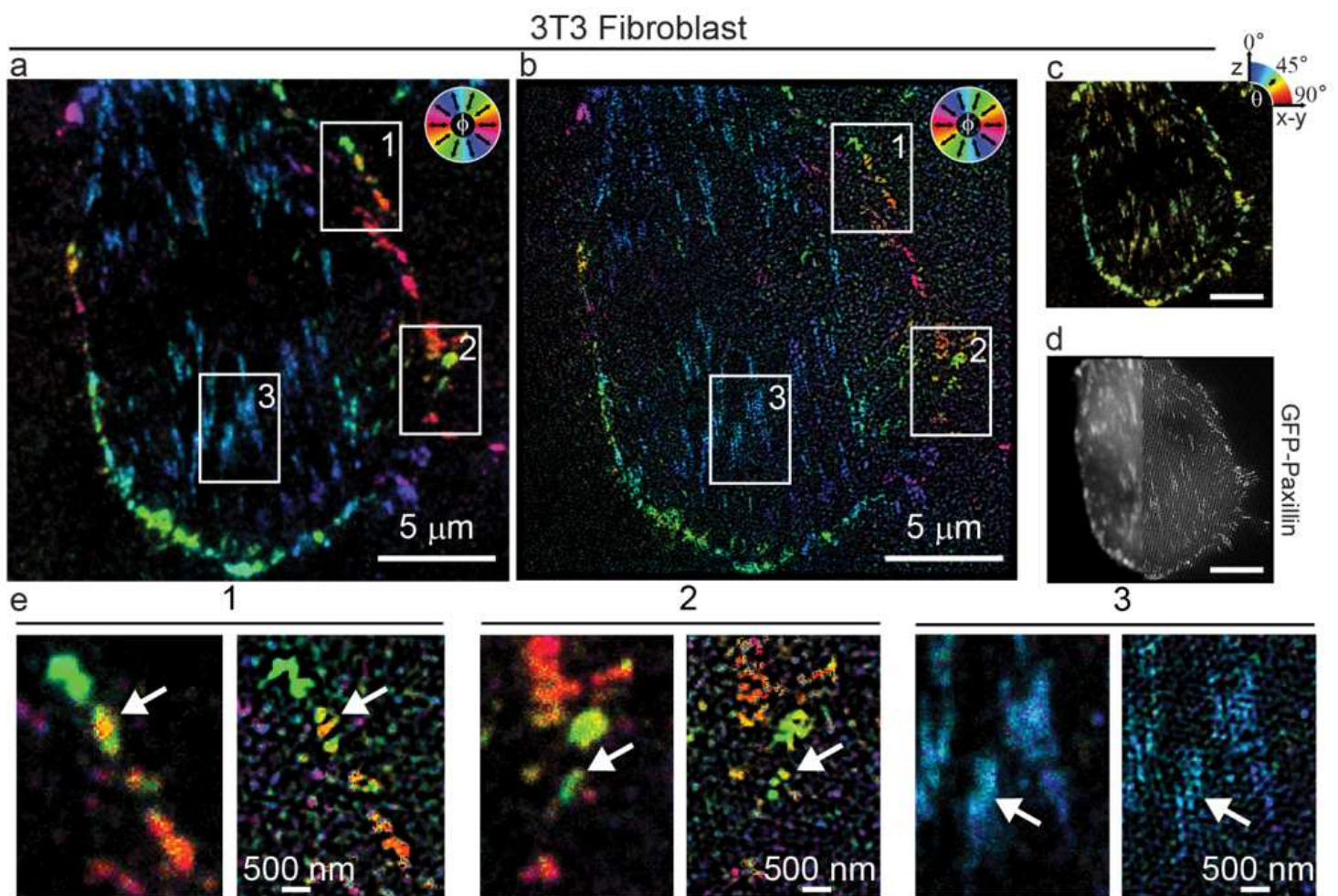


Figure 3

Representative 3T3 fibroblast data. a-c) Colormap-based display of orientation of integrin forces applied by an NIH 3T3 mouse fibroblast cell. ϕ -colored fluorescence images in a) widefield and b) super-resolution, as well as a c) widefield θ -colored image, are shown. d) GFP-tagged paxillin (an FA protein) is shown in widefield and super-resolution. e) Three zoom-ins denoted in a and b show FA structures (some

denoted using white arrows) that can be resolved using super-resolution SIM-MFM that would otherwise appear to be blurred together using widefield MFM. Scale bars are 5 μm for full-cell images, 500 nm for zoom-in images.

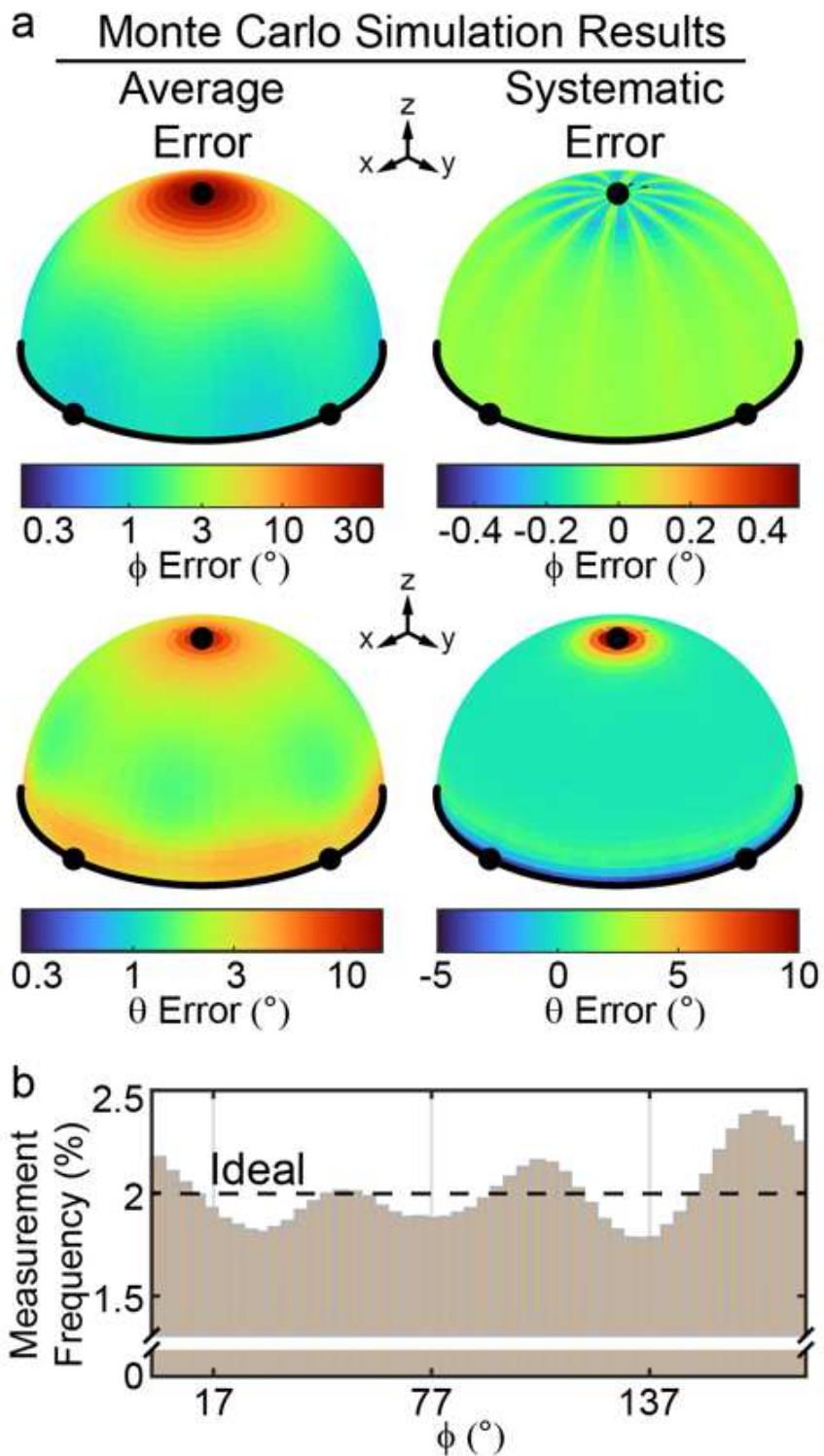


Figure 4

Analysis of measurement errors. a) Results of Monte Carlo simulations of force orientation measurement. Four unit hemispheres are shown. The color of each point on a hemisphere denotes the

error of the orientation that passes through that point. Average error (left) and systematic error (right) are shown for φ (top) and θ (bottom). b) Histogram of all φ values accumulated from 81 platelet timelapses. Dashed line shows the ideal behavior (2% measurement frequency in each of 50 bins). Small variations (from 1.81% to 2.16%) reveal a small effect of systematic errors. Only the brightest 50% of pixels were included in the analysis.

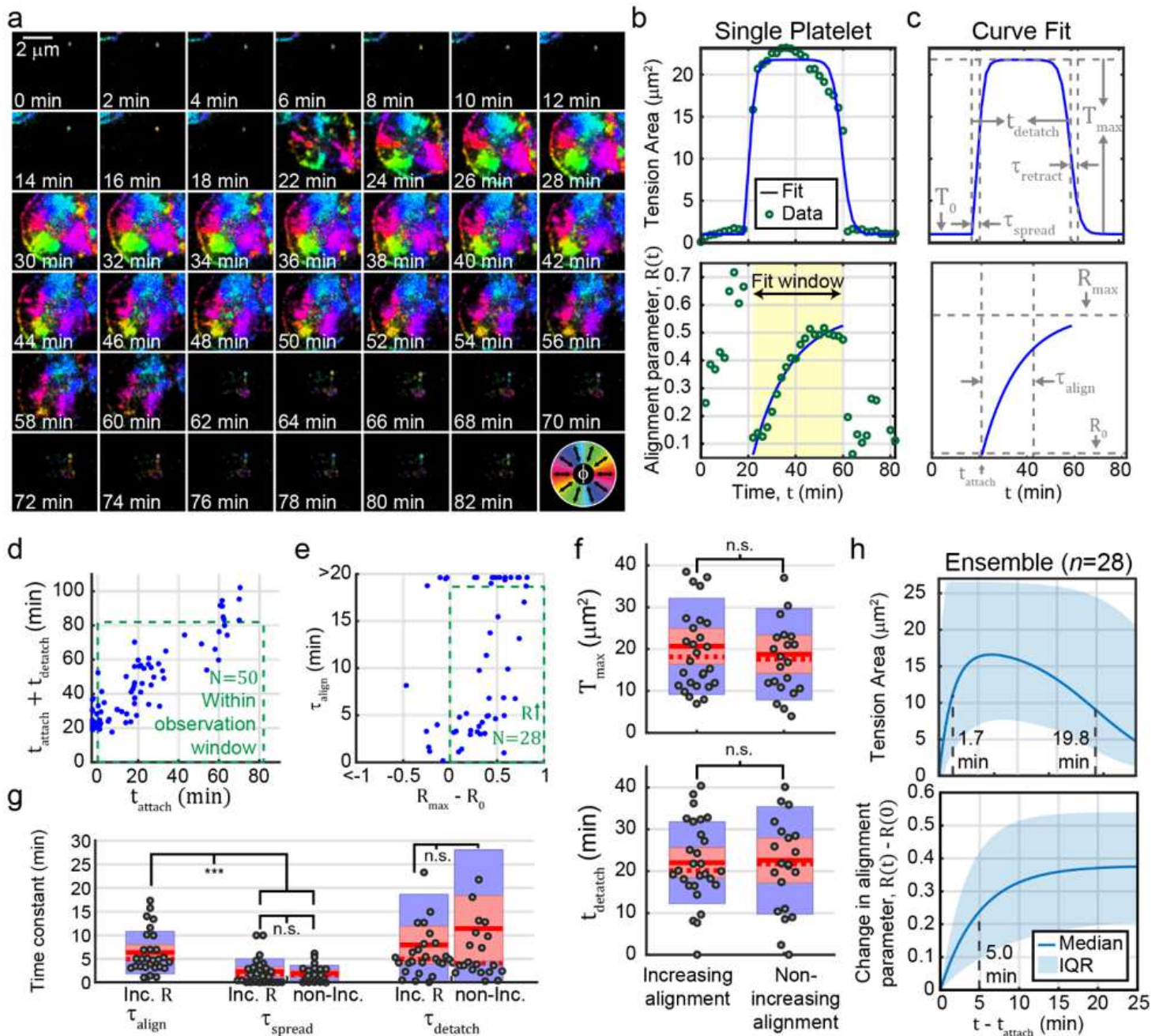


Figure 5

Dynamic properties of human platelets revealed using SIM-MFM. a) Timelapse of a platelet spreading on a surface, shown using the φ -colormap display method (see color wheel in bottom right corner). Gradual tension alignment can be seen via careful inspection; greens and cyans are common at early timepoints, but gradually transition to purple and dark blue due to alignment of platelet tension. b) Tension area (top)

and the alignment parameter (bottom), R , quantified as a function of time, t , with curve fits shown (blue). Yellow shading denotes time window of platelet attachment. c) Best-fit curves from b with annotations depicting fit parameters. d) scatterplot of best-fit $t_{\text{attach}}+t_{\text{detach}}$ (the timepoint at which platelet detachment occurs) and t_{attach} (the timepoint at which attachment occurs) values. Green dashed line shows the parameter space in which attachment and detachment both occurred within the duration of the timelapse. e) Scatterplot of best-fit τ_{align} (the time constant for tension alignment) and ΔR (the change in alignment) values for the platelets selected from d. Green line shows selected population with increasing alignment. f) Boxplots of T_{max} (the max platelet spread area – top) and t_{detach} (the duration of platelet attachment – bottom) for the 28 cells selected in e. Solid red line indicates mean, dashed red line indicates median, red boxes show standard error of the mean and blue boxes shows 95% confidence interval of the mean. Grey circles indicate individual datapoints. g) Boxplots for τ_{align} , τ_{spread} (the time constant for platelet spreading), and τ_{detach} (the time constant for platelet retraction). *** denotes $p < 0.001$, and n.s. denotes $p > 0.05$ (Wilcoxon rank-sum test for difference in population medians). h) Depiction of ensemble behavior. Blue curves denote reconstruction with median best-fit parameters and blue shading denote range of values obtained using all possible combinations of 25th, 50th, and 75th percentile best-fit parameters.

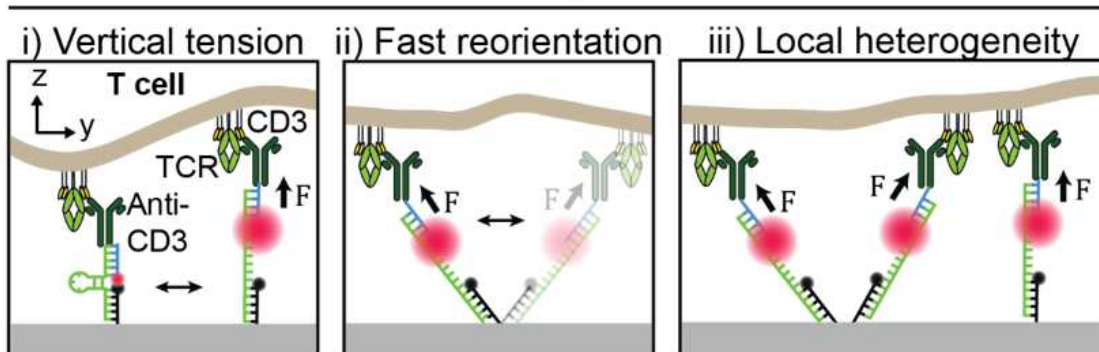
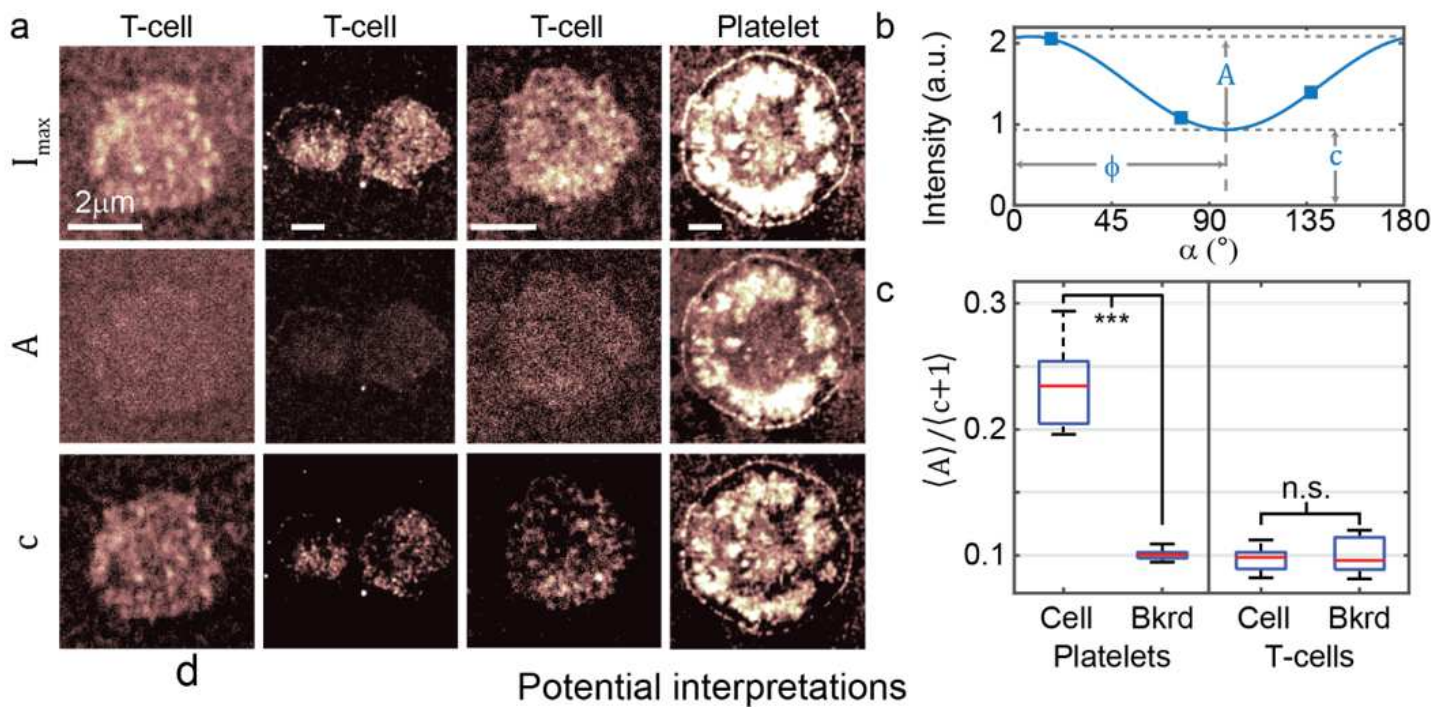


Figure 6

Analysis of T-cell receptor tension reveals no polarization-dependence a) Three example T-cells and one platelet are shown in three panels each. The top row shows I_{\max} , the second row shows the polarization-dependent component of the fit sinusoid, A , and the third row shows the polarization independent component of the fit sinusoid, c . While platelets display substantial polarization dependence (high A), T-cells exhibit almost no polarization dependence (low A) b) A fit sinusoid is shown with A and c depicted (adapted from Fig. 1c). c) A quantification of the polarization response, $A/(c+1)$ (the averaged polarization-dependent component divided by the average polarization-dependent component of the fit sinusoids) of several ($N>25$) T-cells and platelets, both under the cell and in the surrounding background close to the cell. While platelets exhibit a much higher polarization response than the background signal, T-cells do not. d) Three potential causes of the lack of polarization response in T-cells. TCR forces may be some combination of i) vertical to the glass surface, ii) highly dynamic such that the orientation of each open tension probe is randomized during the ~ 100 ms exposure time of each image, and iii) locally heterogenous such that neighboring probes obfuscate each others' polarization responses. All three of these scenarios can result in the lack of polarization response observed.

Supplementary Files

This is a list of supplementary files associated with this preprint. Click to download.

- [SISIMMFMSubmissionSep25.docx](#)